


ORIGINAL ARTICLE

Open Access



Material Removal Mechanism and Force Modeling in Ultrasonic Vibration-Assisted Micro-Grinding Biological Bone

Jingang Sun¹, Changhe Li^{1*} , Zongming Zhou², Bo Liu³, Yanbin Zhang¹, Min Yang¹, Teng Gao¹, Mingzheng Liu¹, Xin Cui¹, Benkai Li¹, Runze Li⁴, Yusuf Suleiman Dambatta^{1,5} and Shubham Sharma^{1,6}

Abstract

Micro-grinding with a spherical grinding head has been deemed an indispensable method in high-risk surgeries, such as neurosurgery and spine surgery, where bone grinding has long been plagued by the technical bottleneck of mechanical stress-induced crack damage. In response to this challenge, the ultrasound-assisted biological bone micro-grinding novel process with a spherical grinding head has been proposed by researchers. Force modeling is a prerequisite for process parameter determination in orthopedic surgery, and the difficulty in establishing and accurately predicting bone micro-grinding force prediction models is due to the geometric distribution of abrasive grains and the dynamic changes in geometry and kinematics during the cutting process. In addressing these critical needs and technical problems, the shape and protrusion heights of the wear particle of the spherical grinding head were first studied, and the gradual rule of the contact arc length under the action of high-speed rotating ultrasonic vibration was proposed. Second, the mathematical model of the maximum thickness of undeformed chips under ultrasonic vibration of the spherical grinding head was established. Results showed that ultrasonic vibration can reduce the maximum thickness of undeformed chips and increase the range of ductile and bone meal removals, revealing the mechanism of reducing grinding force. Further, the dynamic grinding behavior of different layers of abrasive particles under different instantaneous interaction states was studied. Finally, a prediction model of micro-grinding force was established in accordance with the relationship between grinding force and cutting depth, revealing the mechanism of micro-grinding force transfer under ultrasonic vibration. The theoretical model's average deviations are 10.37% in x-axis direction, 6.85% in y-axis direction, and 7.81% in z-axis direction compared with the experimental results. This study provides theoretical guidance and technical support for clinical bone micro-grinding.

Keywords Spherical grinding head, Gradual contact arc length, Maximum undeformed chip thickness, Micro-grinding force

*Correspondence:

Changhe Li
sy_lichanghe@163.com

Full list of author information is available at the end of the article



© The Author(s) 2023. **Open Access** This article is licensed under a Creative Commons Attribution 4.0 International License, which permits use, sharing, adaptation, distribution and reproduction in any medium or format, as long as you give appropriate credit to the original author(s) and the source, provide a link to the Creative Commons licence, and indicate if changes were made. The images or other third party material in this article are included in the article's Creative Commons licence, unless indicated otherwise in a credit line to the material. If material is not included in the article's Creative Commons licence and your intended use is not permitted by statutory regulation or exceeds the permitted use, you will need to obtain permission directly from the copyright holder. To view a copy of this licence, visit <http://creativecommons.org/licenses/by/4.0/>.

1 Introduction

With the development of medical engineering technology, micro-trauma and rehabilitation have become one of the development directions of surgery [1, 2], and micro-grinding of bone materials has become a hot topic of scholars [3–6]. Micro-scale grinding mainly refers to the direct mechanical removal process using a micro-abrasive tool with a processing feature size of less than 50 μm [7]. It has the advantages of high processing precision and suitability for processing hard and brittle materials [8–11]. Therefore, it is increasingly applied in bone surgery to achieve the removal of bone tissue. However, a major challenge in orthopedics is the bottleneck caused by crack damage caused by mechanical stress during grinding. Controlling the cracks within the self-healing range of the bone and ensuring that the bone is not damaged become crucial to avoid any form of secondary damage to the bone material and shorten the patient's recovery time [12–14]. Therefore, before the actual processing, predicting the grinding force during the processing is necessary.

The grinding force of bone materials is mainly studied from two aspects: cutting parameters and grinding mechanism. Zhu et al. [15] and Babbar et al. [16] studied the rule of influence of cutting parameters on grinding force. Experiments showed that the grinding force of bone material increased with the increase in workpiece moving speed and grinding depth, and the grinding force can be effectively reduced by increasing the rotation speed of grinding wheel and increasing the particle size. Zhang et al. [17] analyzed the degree of influence of grinding parameters on tangential force and normal force, and found that the component force in both directions can increase with the increase in feed speed and cutting depth. Meanwhile, the increase in rotational speed was conducive to the reduction in grinding force. Speed has the greatest influence on tangential force, followed by cutting depth and feed speed, whereas normal force is cutting depth > speed > feed speed. Yang et al. [18] established a semi-empirical heat flux model for toughness micro-grinding of hard brittle bone materials by using the grinding force measured during the grinding of bone materials with a spherical grinding head under high-speed rotation. They pointed out that the removal methods of bone materials in the grinding process are mainly divided into ductile removal, powder removal, and brittle fracture removal. In terms of establishing a grinding force model on the basis of a grinding mechanism, Zou et al. [19] used a single abrasive particle as the research object and successfully established a grinding force model of ball-end grinding tools through the application of specific grinding energy and material removal rate. Then, a 3D grinding force prediction model was

fitted by cutting test. Tian et al. [20] regarded the abrasive grain as a conical table perpendicular to the workpiece surface and calculated the cutting depth in the cutting force model. Assuming that the cutting depth is greater than the minimum non-deformation cutting depth, tangential force and normal force were determined by Merchant shear theory. Then, the cutting force and cutting temperature models of micro-grinding were established on the basis of which finite element analysis was carried out to simulate the changing trend of grinding force under different cutting depths or directions.

A large number of studies showed that ultrasonic-vibration-assisted grinding (UVAG) can remarkably reduce grinding force compared with conventional grinding (CG) [21–23]. At present, the research on grinding force modeling of UVAG mainly focuses on two typical machining modes for cylindrical grinding heads: ultrasonic-vibration-assisted end grinding (UVAEG) [24–27] and ultrasonic-vibration-assisted side grinding (UVASG) [28–30]. Li et al. [31] studied the conical grinding head and successfully established a theoretical model of normal grinding force. However, most of these studies do not take into account the protrusion height of abrasive particles and the random distribution of abrasive particles, which can have a significant effect on the behavior of grinding forces. Therefore, future studies should address these factors to gain a more complete understanding of grinding force analysis in orthopedics.

However, compared with cylindrical grinding heads, spherical grinding heads have several advantages in bone grinding. First, the spherical face enables multi directional cutting, which better adapts to complex bone shapes, especially when dealing with curved surfaces or special requirements. Therefore, the machining accuracy is higher. In addition, the small vibration caused by ultrasonic waves of the spherical grinding head plays a crucial role in the grinding process. These vibrations can effectively prevent the adhesion and clogging of the grinding surface, thereby reducing the change in cutting force and the accumulation of friction heat [32]. As a result, the stability and efficiency of grinding are significantly improved. The cutting force is evenly distributed when it is in contact with the workpiece because the surface of the spherical grinding head is circular, thus improving the cutting stability. This feature helps extend the service life of the grinding head. In summary, the micro-grinding technique using a spherical grinding head has proven to be particularly suitable for high-risk procedures, such as neurosurgery and spinal surgery, where precision, adaptability and stability are key factors.

The effectiveness of UVAG with a spherical grinding head for bone material processing has been experimentally verified by Yang et al. [33]. However, the

underlying principle behind this improvement remains unclear. Establishing the mechanism and force model of ultrasonic-vibration-assisted biologic bone material removal using a spherical grinding head, specifically tailored to match the requirements of actual bone surgery, is urgently needed.

The accuracy of predicting the grinding force model was improved to reveal the material removal mechanism of ultrasonic vibration assisted micro-grinding of biological bone, and the mechanism of grinding force transfer and reduction. First, the geometric characteristics of single particle and spherical grinding head were analyzed, and the average value of the protrusion height based on Rayleigh distribution was obtained. The maximum undeformed chip thickness model of spherical grinding head under ultrasonic vibration was established on the basis of the changing rule of contact arc length at different diameters of spherical grinding head. Through kinematic analysis, the instantaneous interaction stage of abrasive particles was determined, and the mechanism of bone material removal in ductile domain, bone meal, and brittle domain removal stages was revealed. Then, in accordance with the relationship between the grinding force and cutting depth of single diamond in different layers, a dynamic grinding force prediction model of different layers of abrasive particles in different instantaneous interaction states was established. Finally, the total grinding force in the effective grinding zone was obtained by superimposing the overall micro-cutting force vector of all the effective grinding particles. The grinding force prediction model of x , y and z axes was obtained by calculus. The modeling process is shown in Figure 1. This study could provide theoretical basis for accurately predicting the grinding force of bone surgery and inhibiting mechanical stress crack damage.

2 Material Removal Mechanism

The geometry and kinematics under ultrasonic-vibration-assisted micro-grinding were modeled and simulated by Matlab to reveal the material removal mechanism of ultrasonic assisted micro-grinding of biological bone with a spherical grinding head. The effects of vibration direction, grinding tool rotation, vibration parameters and grinding parameters on the geometry and kinematics of abrasive particles were analyzed.

2.1 Geometric Analysis

UVAG is a complex process containing a large number of diamond abrasive grains. Individual diamond abrasive grains were first analyzed to simplify the modeling process, and then the following assumptions and simplifications were given when modeling the cutting forces:

1. The diamond abrasive particles are assumed to be rigid octahedrons, with each particle forming a pyramid by having four neighboring triangles with a common vertex. During the cut, only one pyramid of each octahedral particle is engaged, whereas the other remains buried in the matrix and plating, as depicted in Figures 2(a) and (b).
2. The angle between the opposite edges of the diamond abrasive particles is denoted as 2θ ($2\theta=90^\circ$) [29], and the wear of the diamond abrasive particles is not taken into consideration.
3. Throughout the grinding process, the ultrasonic amplitude (A) and frequency (f) are maintained constant.
4. This study focuses solely on the cutting force in the stable grinding stage, because the raw cutting force signal exhibits instability during the grinding process, especially with strong fluctuations during the cut-in and cut-out stages.

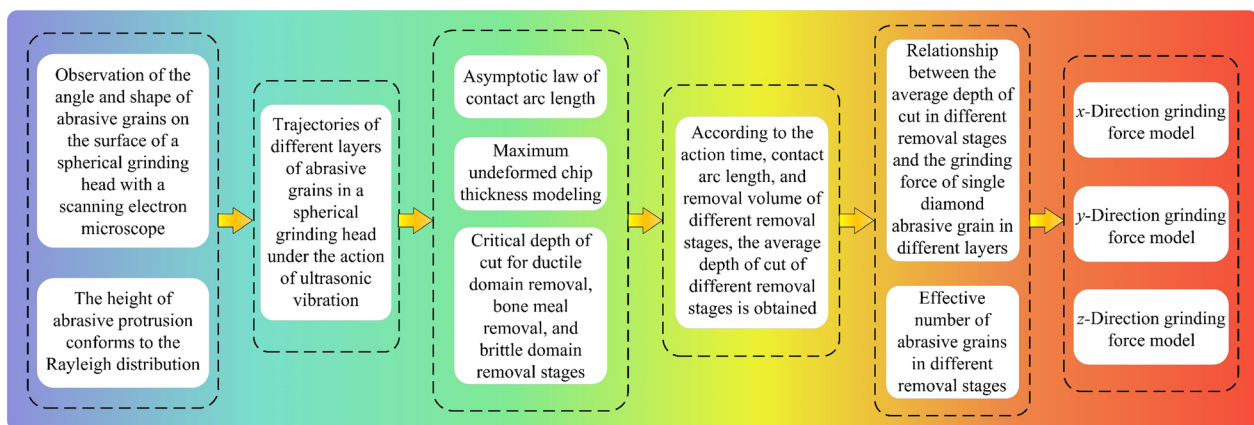


Figure 1 Illustrations of modeling procedures

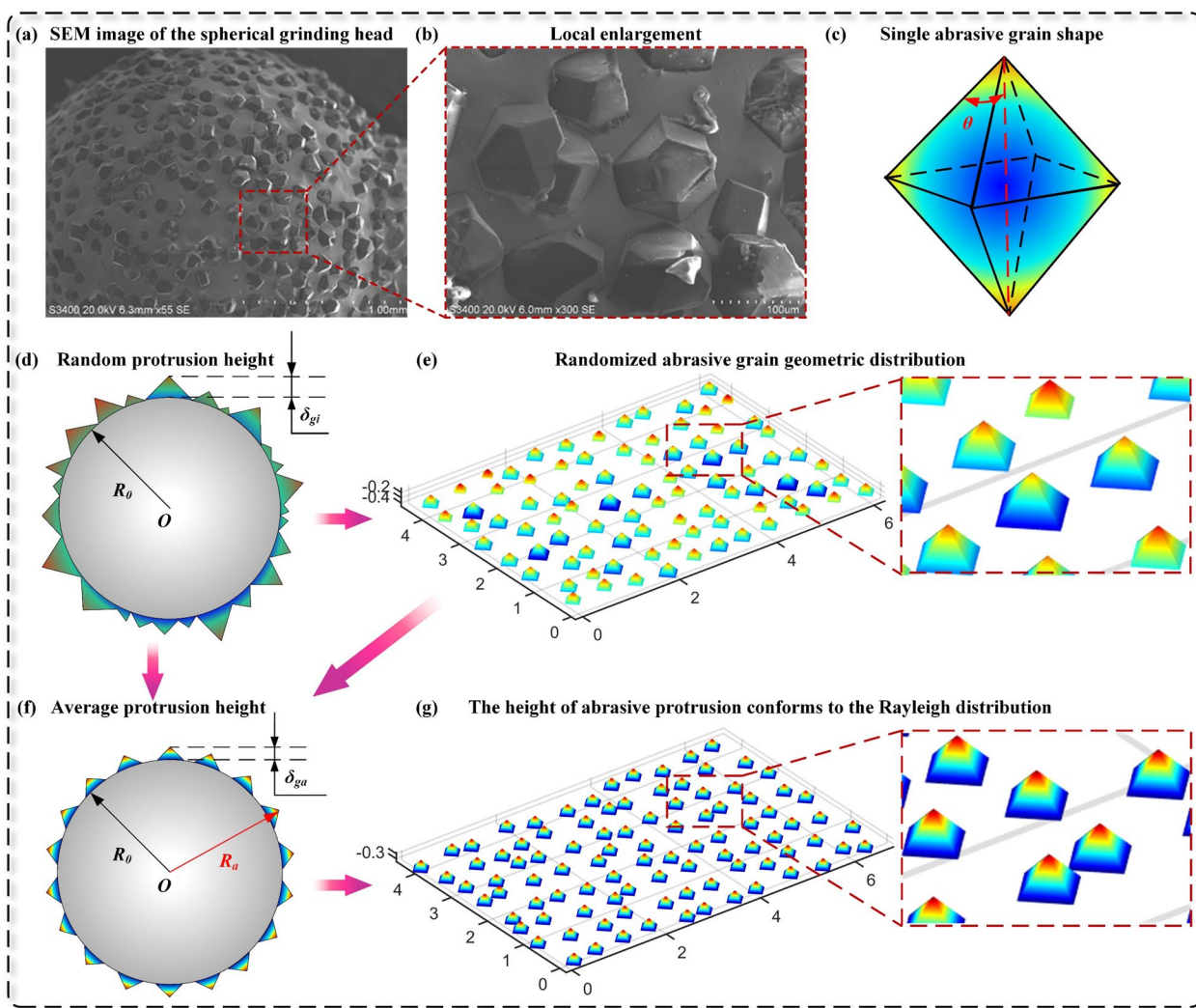


Figure 2 Surface morphology of a spherical grinding head based on random abrasive grain geometry features

2.1.1 Spherical Grinding Head Surface Topography Modeling

The shape of abrasive particles plays an important role in the grinding process and profoundly affects the prediction of grinding force [34]. Therefore, determining the shape of abrasive particles is necessary.

The abrasive grains of the diamond spherical grinding head employed in this study exhibit a random distribution on the spherical surface, with uneven protrusion heights [35–37]. This characteristic exerts a significant effect on the trajectory of the abrasive grains and their depth of penetration into the workpiece, ultimately influencing the grinding force. Consequently, when observing the diamond abrasive grains of the spherical grinding head through scanning electron microscopy (SEM), their shape closely resembles the octahedron depicted in Figure 2(c). On the basis of the analysis of the abrasive grain shape, size, and position, a model for

the random surface morphology of the spherical grinding head was established, as depicted in Figures 2(d) and (e).

A probability density function is required to characterize the random protruding heights of diamond particles to facilitate a more comprehensive analysis of the interaction between diamond particles and the workpiece [38–40]. Wu et al. [38] indicated that the height of protrusion of diamond particles on the surface of the abrasive tool follows the Rayleigh distribution.

$$f(\delta_{gi}) = \begin{cases} (\delta_{gi}/\beta^2)e^{-(\delta_{gi}^2/2\beta^2)}, & \delta_{gi} \geq 0, \\ 0, & \delta_{gi} < 0, \end{cases} \quad (1)$$

In the probability density function, β represents a parameter, and δ_{gi} denotes the random protrusion height of the diamond particles.

$$R_a = R_0 + \delta_{ga}, \quad (2)$$

where O is the center of the abrasive tool; R_a is the average radius used to calculate the spherical abrasive head; R_0 is the radius of the spherical abrasive head base, and δ_{ga} is the average protruding height of diamond abrasive grains, as shown in Figure 1(f). According to the probabilistic statistical method, δ_{ga} can be obtained from the expectation and variance of the Rayleigh function as follows:

$$\begin{cases} E(\delta_{gi}) = \beta \sqrt{\frac{\pi}{2}} \approx 1.253\beta, \\ Var(\delta_{gi}) = \left(2 - \frac{\pi}{2}\right)\beta^2 \approx 0.429\beta^2, \\ E(\delta_{gi}^2) = \int_0^\infty \delta_{gi}^2 f(\delta_{gi}) d\delta_{gi}. \end{cases} \quad (3)$$

Substituting Eq. (1) into Eq. (2) gives the following:

$$E(\delta_{gi}^2) = \left[e^{-\delta_{gi}^2/2\beta^2} (-2\beta^2 - \delta_{gi}^2) \right]_0^\infty = 2\beta^2. \quad (4)$$

The total volume of all diamond particles removed should be equal to the volume removed by the grinding process [41], and it can be expressed as follows:

$$E(\delta_{gi}^2) = \frac{a_e v_\omega}{C_e l_c v_s \tan \theta}, \quad (5)$$

where a_e is the grinding width, mm; v_ω is the feed rate, mm/s; C_e is the number of active diamond grains per square millimeter ($C_e=5$ in this paper); v_s is the cutting speed of individual diamond grains, mm/s; and l_c is the geometric contact arc length between the abrasive and the workpiece, $l_c = \pi a_e$.

Thus, δ_{ga} can be obtained as follows:

$$\delta_{ga} = E(\delta_{gi}) = \sqrt{\frac{\pi a_e v_\omega}{4 C_e l_c v_s \tan \theta}}. \quad (6)$$

After the random protrusion heights of the abrasive grains were averaged, the diamond grains on the abrasive head, which were initially randomly distributed, assumed uniform heights, as illustrated in Figures 2(f)–(g). This simplification results in a more straightforward representation of the grinding behavior arising from the random protrusion heights. The approach adopted in the present study aligns more closely with the actual grinding situation than those in the studies conducted by Yao et al. [24] and Zhang et al. [42, 43], where the assumption of uniform distribution of abrasive grains was employed.

2.1.2 Mechanism of Change in Actual Contact Radius

The actual grinding depth D_p under the action of ultrasonic vibration of the spherical grinding head is as follows:

$$D_p = a_p + A \sin(2\pi ft), \quad (7)$$

where a_p is the grinding depth without ultrasonication, μm .

As shown in Figure 5(a), the number of abrasive layers without ultrasound can be expressed as follows:

$$L_e = \arccos\left(\frac{R_a - a_p}{R}\right) \cdot \frac{R_a}{L}. \quad (8)$$

The number of abrasive layers when adding ultrasound L_{e-U} is obtained as follows:

$$L_{e-U} = \arccos\left(\frac{R_a - D_p}{R}\right) \cdot \frac{R_a}{L}, \quad (9)$$

where L is the distance between adjacent abrasive grains on the surface of the spherical grinding head, μm . It is taken as 25% of the average grain size [18, 44].

The angle $\alpha_i(m)$ corresponding to the different layers of abrasive grains from the bottom of the grinding head to the position parallel to the machined surface is as follows:

$$\alpha_i(m) = m \cdot \frac{L}{R_a}. \quad (10)$$

Considering the grinding surface is in a simple harmonic motion trajectory when ultrasound is added, the value of m takes the range of $1-L_e$.

The radii $R_i(m)$ corresponding to different $\alpha_i(m)$ are as follows:

$$R_i(m) = R_a \cdot \sin[\alpha_i(m)], \quad (11)$$

where $R_i(m)$ is the radius of rotation of the different layers of abrasive grains, mm.

2.2 Kinematic Analysis

2.2.1 Kinematic Analysis of Different Layers of Abrasive UVAG

The motion characteristics of UVAG with a spherical grinding head were analyzed to elucidate the removal mechanism between the grinding head and the biological bone material. The motion of the diamond abrasive grains comprises three main components: high-speed rotation of the spindle, ultrasonic vibration of the spindle, and the horizontal feeding motion of the 3D displaced working platform, as illustrated in Figure 3(a). Initially, the motion

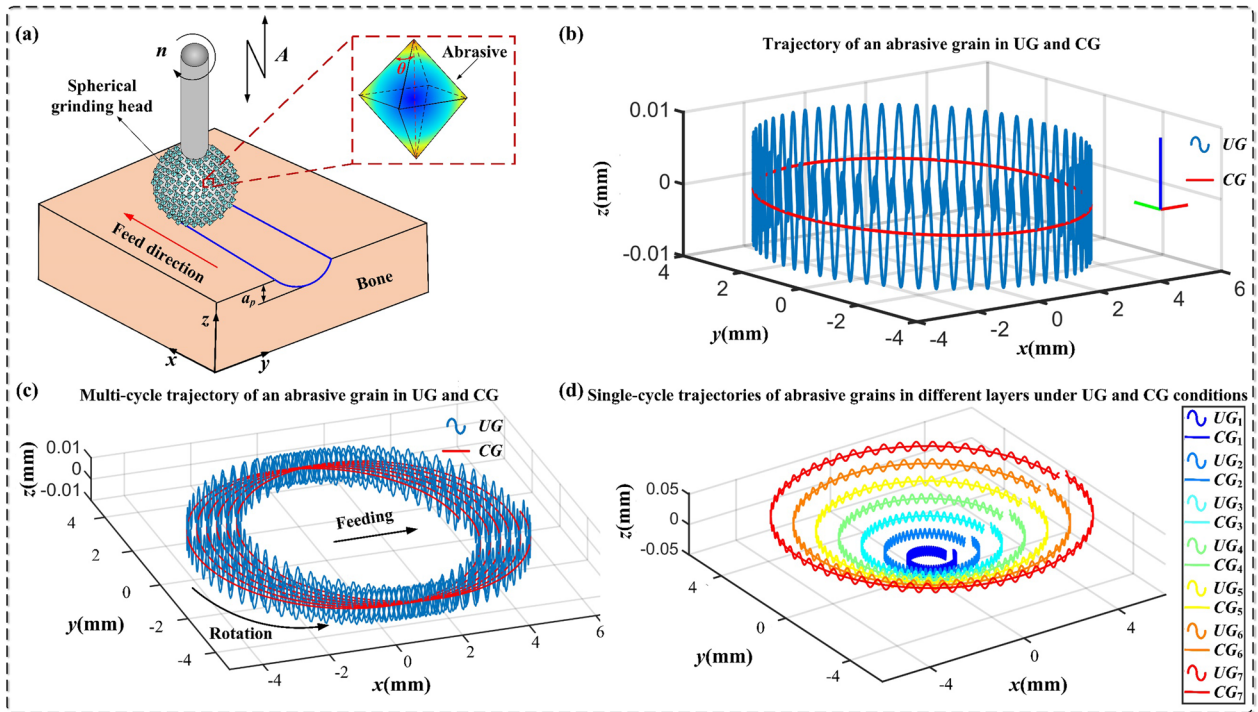


Figure 3 Motion trajectory of diamond abrasive grains on the surface of spherical grinding head under the action of ultrasonic vibration

trajectory of a single diamond abrasive grain was investigated, as shown in Figure 3(b). The motion trajectory of a single diamond abrasive grain with multiple cycles is depicted in Figure 3(c). Additionally, the motion trajectories at different contact radius positions of the spherical grinding head were examined, as illustrated in Figure 3(d). Consequently, the kinematic equations governing the motion of different layers of diamond grains on the surface of UVAG with a spherical grinding head can be expressed as follows:

$$\begin{cases} x(t) = R_i(m) \cos \omega t + v_\omega t, \\ y(t) = R_i(m) \sin \omega t, \\ z(t) = A \cos (2\pi f t). \end{cases} \quad (12)$$

where $R_i(m)$ is the rotational radius of different layers of abrasive grains in the spherical grinding head, mm; $\omega = 2\pi n/60$ rotational angular velocity, rad/s; n is the spindle rotational speed, r/min; f is the ultrasonic frequency, Hz; A is the ultrasonic amplitude, taking the range of values: 2–8 μm ; v_ω is the feed speed, mm/s; and t is the grinding time, s. The grinding time is the time required for grinding process.

The velocity analysis of single abrasive grains at different contact radius locations can be performed as follows:

$$\begin{cases} v_x = -\omega R_i(m) \sin \omega t + v_\omega, \\ v_y = \omega R_i(m) \cos \omega t, \\ v_z = -2\pi f A \sin (2\pi f t). \end{cases} \quad (13)$$

2.2.2 Asymptotic Contact Arc Length

An arbitrary $a_i(m)$ in the absence of ultrasonic vibrations corresponds to an asymptotic geometric contact arc length of half a rotation period as follows:

$$l_{c_si}(m) = \pi R_i(m). \quad (14)$$

Any $a_i(m)$ in the absence of ultrasonic vibrations corresponds to an asymptotic motion contact arc length of half a rotation period as follows:

$$l_{c_ci}(m) = \int_0^{\frac{30}{n}} \sqrt{v_x^2 + v_y^2} dt. \quad (15)$$

The asymptotic kinematic contact arc length for half a rotation cycle under ultrasonic vibration is given as follows:

$$l_{c_ui}(m) = \int_0^{\frac{30}{n}} \sqrt{v_x^2 + v_y^2 + v_z^2} dt. \quad (16)$$

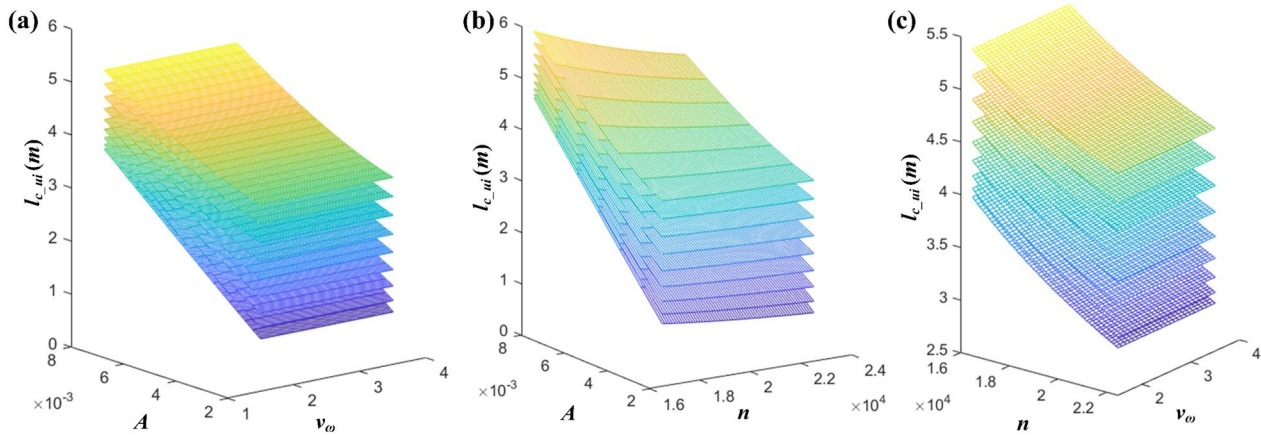


Figure 4 Asymptotic law of contact arc length of spherical grinding head motion under the action of ultrasonic vibration

As shown in Figure 4, under the action of ultrasonic vibration, the relationship between any $a_i(m)$ corresponding to the continuous contact arc length not only depends on the rotation radius $R_i(m)$ of different layers of abrasive particles, but also is affected by the amplitude A , spindle speed n , and feed speed v_ω . The contact arc length of the spherical grinding head increases gradually from the bottom end of the grinding head to the unprocessed surface of biological bone under the action of rotating ultrasonic vibration. The contact arc length of each layer increases with the increase in amplitude. In addition, the larger the amplitude is, the more uniform the change of contact arc length from the bottom to the unmachined surface under ultrasonic vibration. Moreover, and the smaller the amplitude is, the more obvious the gradual difference of contact arc length from the bottom to the unmachined surface under ultrasonic vibration.

2.2.3 Asymptotic Modeling of Maximum Undeformed Chip Thickness

The brittle domain removal range of the spherical grinding head is determined by the feed distance S , and the predictive model for lateral grinding of cylindrical grinding heads relies on the maximum undeformed chip thickness to establish the brittle domain removal range [42]. Under the same machining conditions, the feed distance S remains constant for different layers of the spherical grinding head. It is equal to the maximum undeformed chip thickness of each layer multiplied by the number of static effective abrasive grains in the corresponding layer. As a result, the maximum undeformed chip thickness varies among different layers of the spherical grinding head under the same machining conditions, as depicted in Figure 5(d).

In the absence of ultrasound, the maximum undeformed chip thickness corresponding to each layer can be determined as follows:

$$h_{u_ci}(m) = \frac{L}{v_s} v_\omega = \frac{30Lv_\omega}{\pi n R_i(m)}. \tag{17}$$

Under the effect of ultrasonic vibration, the maximum undeformed chip thickness of a spherical grinding head can be obtained as follows:

From a macroscopic perspective, the final material removal remains the same for grinding without ultrasonic vibration and grinding under the effect of ultrasonic vibration [45], i.e., $V_{CG} = V_{UG}$. Consequently, the equation becomes:

$$V_{CG} = \frac{1}{3} \cdot h_{u_ci}^2(m) \cdot \tan \theta \cdot l_{c_ci}(m). \tag{18}$$

The contact arc length of a single abrasive grain under the action of ultrasonic vibration can be expressed as follows:

$$V_{UG} = \frac{1}{3} \cdot h_{u_ui}^2(m) \cdot \tan \theta \cdot l_{c_ui}(m). \tag{19}$$

The maximum undeformed chip thickness corresponding to any $a_i(m)$ under ultrasonic vibration is modeled as follows:

$$h_{u_ui}(m) = \frac{30 \cdot L \cdot v_\omega}{\pi n R_i(m)} \cdot \left[\frac{l_{c_ci}(m)}{l_{c_ui}(m)} \right]^{1/2}. \tag{20}$$

The Matlab simulation results show that the maximum undeformed chip thickness of different layers of the spherical grinding head within the range of different processing parameters selected in the experiment in Table 1 is less than the maximum processing characteristic size of micro-grinding at $50 \mu\text{m}$, so this study is micro-grinding. The gradient rule of the maximum undeformed chip thickness of different layers of the spherical grinding head under different processing

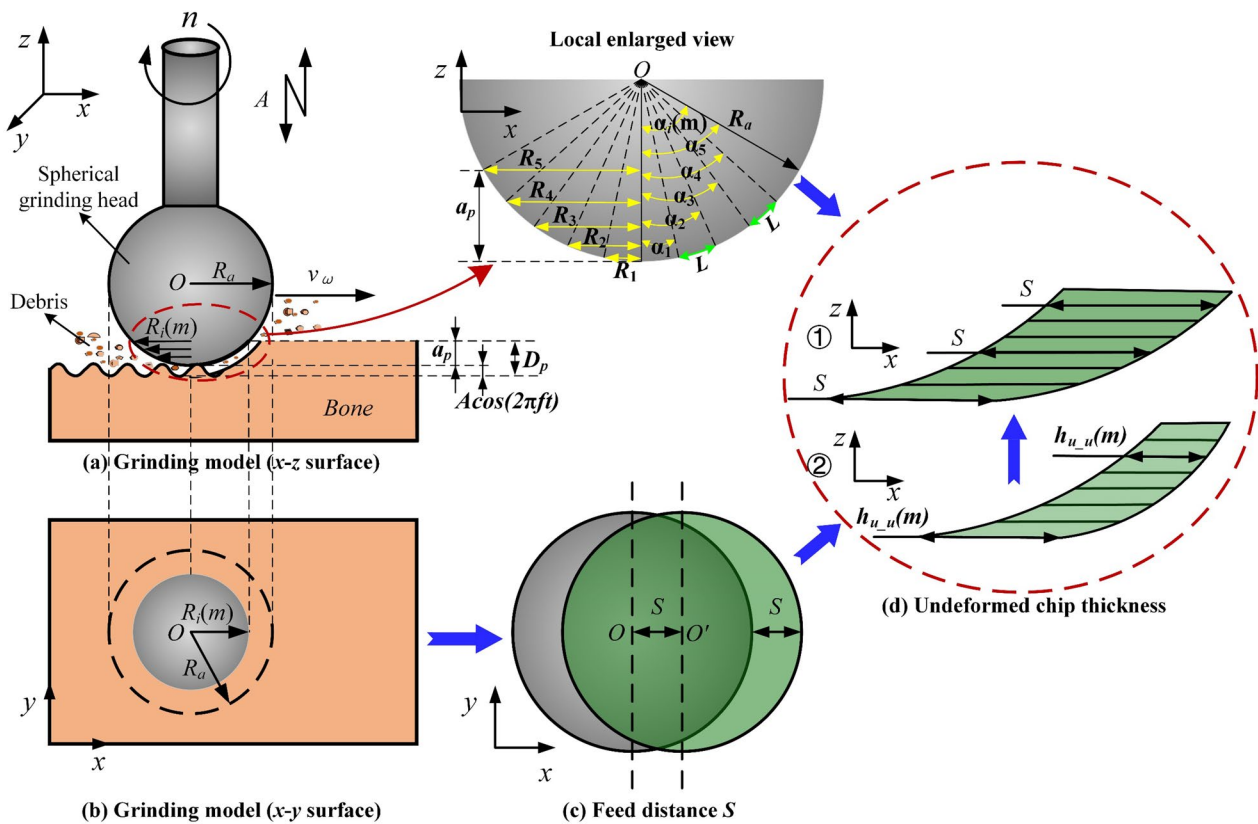


Figure 5 Model of maximum undeformed cutting thickness of different layers of spherical grinding head under ultrasonic vibrations

Table 1 Machining parameters

Experiment No.	Grinding process parameters	Numerical value
1	Spherical grinding head radius R_g (mm)	1.5, 2, 2.5, 3, 3.5
2	Spindle speed n (r/min)	16500, 18000, 19500, 21000, 22500
3	Feed rate v_ω (mm/min)	90, 120, 150, 180, 210
4	Grinding depth a_p (mm)	0.015
5	Amplitude A (μ m)	2–8

parameters selected in the experiment in Table 1 is shown in Figure 6. With the increase in amplitude, the maximum undeformed chip thickness of each layer decreases under the action of ultrasonic wave. In addition, the larger the amplitude is, the more uniform the change of the maximum undeformed chip thickness from the bottom layer to the unmachined surface under ultrasonic vibration. The smaller the amplitude is, the more obvious the gradient difference of the maximum undeformed chip thickness from the bottom layer to the unmachined surface under ultrasonic vibration.

In addition, the maximum undeformed cutting thickness decreases with the increase in $R_i(m)$, and the maximum undeformed chip thickness appears in the layer closest to the bottom layer of the spherical grinding head. Ultrasonic vibration can reduce the maximum thickness of undeformed chips and is more conducive to the removal of biological bone in ductile area.

2.3 Determination Mechanism of Contact Stages

2.3.1 Critical Depth of Cut

The Bifano’s model [46], widely employed in evaluating the ductile to brittle transition during grinding processes of brittle materials [47, 48], can be effectively utilized for biological bone, which is known to be a hard and brittle material [18]. By employing this model, the critical depth of cut h_2 for the bone powder removal stage and the brittle domain removal stage can be determined as follows:

$$h_2 = 0.15 \left(\frac{E}{H_{v-u}} \right) \left(\frac{K_{id}}{H_{v-u}} \right)^2, \tag{21}$$

where E , H_{v-u} , and K_{id} are the modulus of elasticity, the Vickers hardness, and the dynamic fracture toughness of the bone material under the effect of ultrasonic vibration,

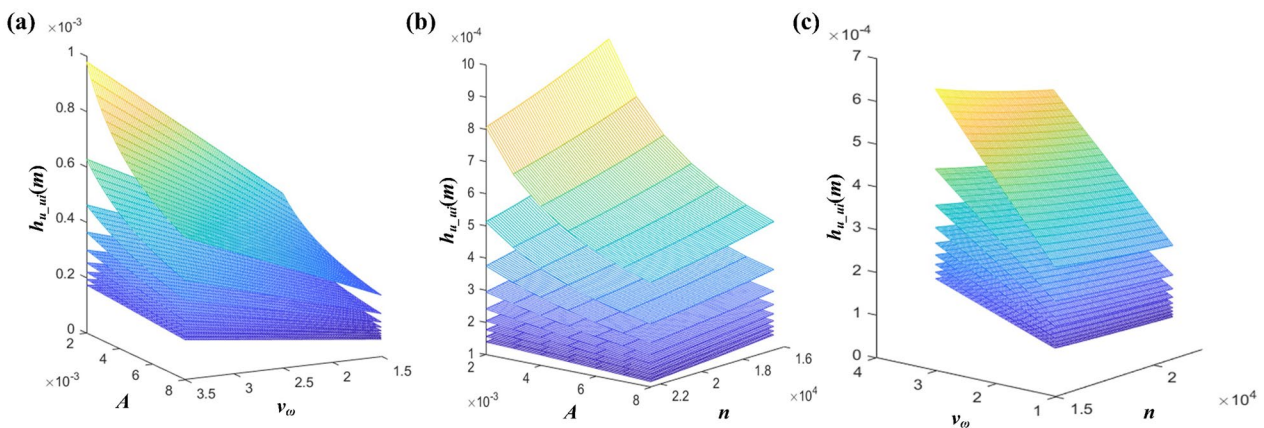


Figure 6 Asymptotic law of maximum undeformed chip thickness with ultrasonic amplitude in different layers of a spherical grinding head under ultrasonic vibrations

Table 2 Basic mechanical properties of dense bone from fresh bovine femur [59–64]

Mechanical property	Numerical value
Modulus of elasticity E (GPa)	17.9
Poisson’s ratio ν	0.33
Vickers hardness H_v (HV)	47
Fracture toughness K_{Ic} (MPa·m ^(1/2))	3.5

respectively, as shown in Table 2. Due to the presence of ultrasonic vibration, the surface hardness of the bone material decreased by 33% with $K_{id} = 0.33K_{ic}$ [49], which is the static fracture toughness, and $H_{v,u} = 0.7H_v$ [50], which is the Vickers hardness of the bone material.

The critical depth of cut h_1 for the ductile domain removal stage and bone meal removal stage is given by:

$$h_1 = \tau h_2, \tag{22}$$

where τ is the coefficient of the ductility phase, which is 0.25 in the present study [42, 51].

2.3.2 Turning Angle and Time Corresponding to the Critical Depth of Cut

The depth of cut is gradually increased from zero to a maximum value and then decreased to zero within a single rotation cycle, being symmetric about the x -axis, as depicted in Figure 7(c). As shown in Figure 7(a), the material is initially removed by plastic flow and further removed by plastic flow and microcrack expansion, resulting in the formation of bone dust, as shown in Figure 7(b). Subsequently, the material is removed by brittle fracture, as shown in Figure 7(d). In the ductile domain removal stage, the grinding time is $2t_1$, the feed

distance is x_1 , and the rotation angle is $2\varphi_1$. In the bone powder removal stage, the grinding time is $2(t_2 - t_1)$, the feed distance is x_2 , and the rotation angle is $2(\varphi_2 - \varphi_1)$. In the brittle domain removal stage, the grinding time is $2(t_3 - t_2)$, the feed distance is S , and the rotation angle is $2(\varphi_3 - \varphi_2)$. The specific derivation is as follows:

$$\left\{ \begin{aligned} x_1 &= v_\omega \cdot t_1 = \frac{h_1}{\sin \varphi_1}, \\ x_2 &= v_\omega \cdot t_2 = \frac{h_2}{\sin \varphi_2}, \\ x_3 &= S = v_\omega \cdot t_3, \\ t_1 \sin \left(\frac{2\pi n t_1}{60} \right) &= \frac{h_1}{v_\omega}, \\ t_2 \sin \left(\frac{2\pi n t_2}{60} \right) &= \frac{h_2}{v_\omega}, \\ t_3 \sin \left(\frac{2\pi n t_3}{60} \right) &= \frac{x_3}{v_\omega}, \\ t_3 &= \frac{30}{\pi n} \arcsin(1), \\ \varphi_1 &= \frac{2\pi n}{60} t_1, \\ \varphi_2 &= \frac{2\pi n}{60} t_2, \\ \varphi_3 &= \frac{2\pi n}{60} t_3 = \frac{\pi}{2}. \end{aligned} \right. \tag{23}$$

2.3.3 Asymptotic Contact Arc Lengths at Different Stages

The cutting lengths of the different layers of single diamond grains during the grinding process can be analyzed by considering only half of the rotational cycle, because the grinding process of the spherical grinding head is symmetrical to the x -axis. This phenomenon facilitates the calculation as follows:

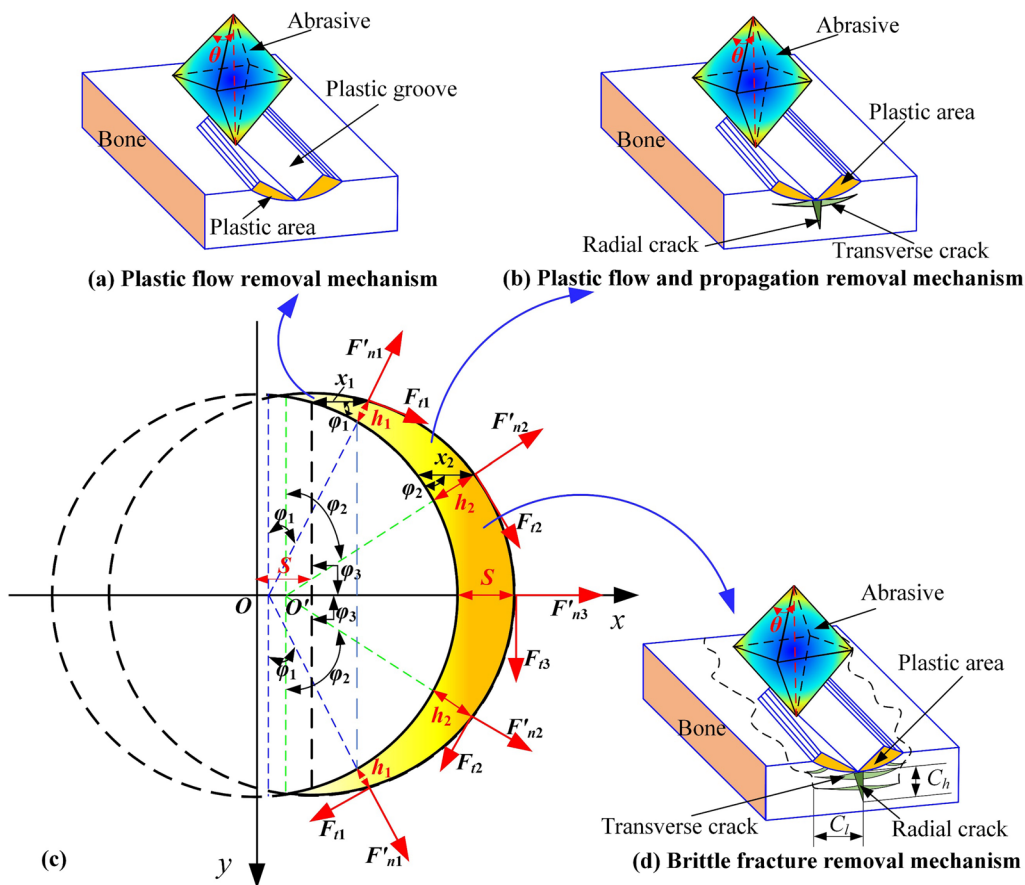


Figure 7 Instantaneous interaction phases and material removal modes of single diamond grains of a spherical grinding head under the action of ultrasonic vibrations

$$\begin{cases} l_1(m) = \int_0^{t_1} \sqrt{v_x^2 + v_y^2 + v_z^2} dt, \\ l_2(m) = \int_{t_1}^{t_2} \sqrt{v_x^2 + v_y^2 + v_z^2} dt, \\ l_3(m) = \int_{t_2}^{t_3} \sqrt{v_x^2 + v_y^2 + v_z^2} dt. \end{cases} \quad (24)$$

2.4 Average Depth of Cut

2.4.1 Ductile Domain Removal Phase

The removal volume and average depth of cut for different layers of single abrasive grains in the ductile domain removal stage when $0 < h_{u1} < h_1$ can be determined. Obtaining the average depth of cut is essential because the depth of cut h_{u1} of a single diamond abrasive grain varies continuously with time during the ductile phase. As illustrated in Figure 8(a), the material removal volume $V_1(m)$ of different layers of single diamond abrasive grain

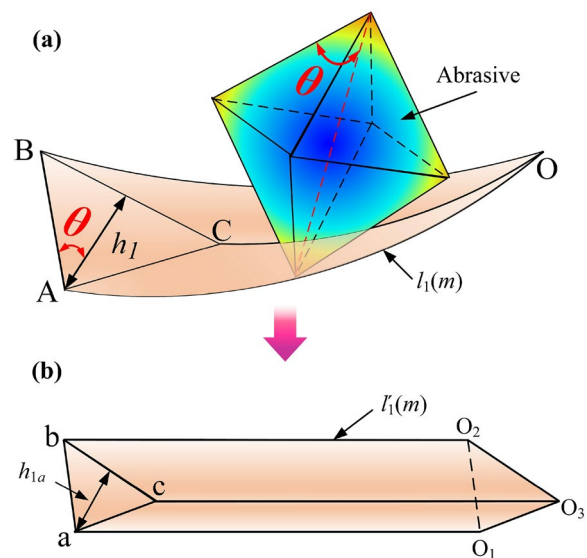


Figure 8 Removal volume and average depth of cut in the ductile domain removal phase

during the removal phase of the ductile domain can be regarded as the volume of a triangular cone, with the following expression:

$$V_1(m) = \frac{l_1(m)}{3} \left(\frac{1}{2} 2h_1 \tan \theta h_1 \right) = \frac{l_1(m)}{3} (h_1^2 \tan \theta). \tag{25}$$

The length $l_1(m)$ represents the trajectory of a single diamond abrasive grain of different layers in the ductile mode during half of a rotation cycle.

The equivalent material removal volume of different layers of single diamond abrasive grain in the ductile domain removal stage can be idealized as a tri-prism with the same cross-sectional area, as shown in Figure 8(b), where the length of the ductile domain trajectory is $l'_1(m)$ and the height is h_{1a} during time $0-t_1$. Therefore, the equivalent volume $V_{1a}(m)$ is given as follows:

$$V_{1a}(m) = l'_1(m) h_{1a}^2 \tan \theta, \tag{26}$$

when $l_1(m) = l'_1(m)$, the average depth of cut $h_{1a}(m)$ in the removal stage of the ductile domain can be obtained from the equation $V_1(m) = V_{1a}(m)$ as follows:

$$h_{1a}(m) = \frac{\sqrt{3}}{3} h_1. \tag{27}$$

2.4.2 Bone Meal Removal Phase

During the bone meal removal stage, when $h_1 < h_{a2} < h_2$, the material removal volume $V_2(m)$ of different layers of single diamond abrasive grains can be obtained using the following expression, as shown in Figure 9(a):

$$\begin{aligned} V_2(m) &= \frac{l_1(m) + l_2(m)}{3} \left(\frac{1}{2} 2h_2 \tan \theta h_2 \right) \\ &\quad - \frac{l_1(m)}{3} (h_1^2 \tan \theta) \\ &= \frac{l_1(m) + l_2(m)}{3} (h_2^2 \tan \theta) \\ &\quad - \frac{l_1(m)}{3} (h_1^2 \tan \theta). \end{aligned} \tag{28}$$

The length of the trajectory of the bone powder removal stage at time t_1-t_2 is $l_2(m)$. Assuming that the equivalent material removal volume of different layers of single diamond abrasive grains is shaped as a triangular prism with the same cross-sectional area, as shown in Figure 9(b), the equivalent volume $V_{2a}(m)$ is given by the following expression:

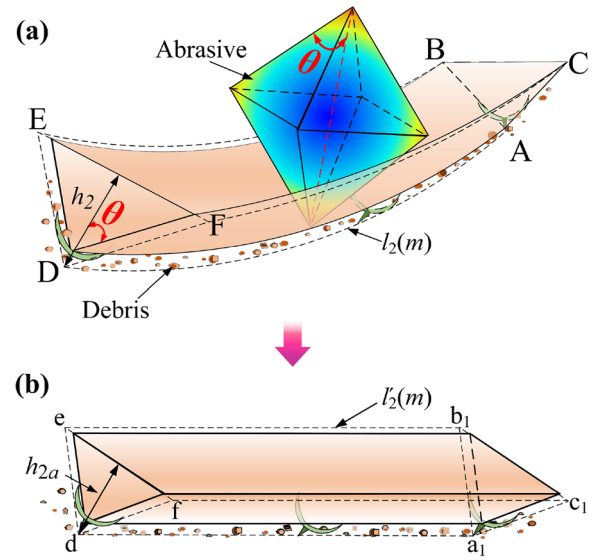


Figure 9 Removal volume and average depth of cut in bone meal removal phase

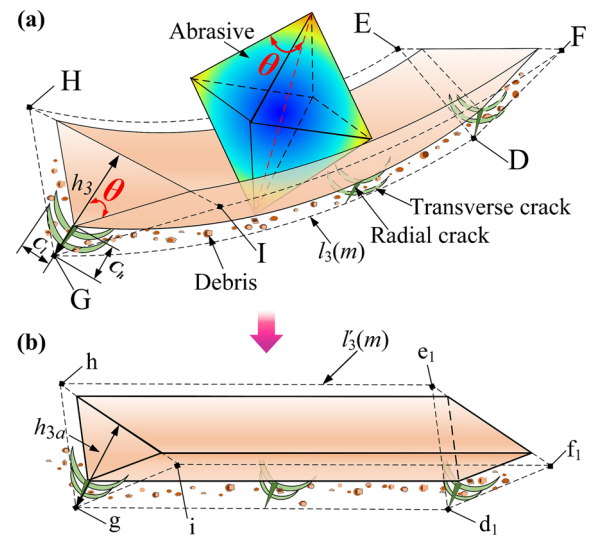


Figure 10 Removal volume and average depth of cut in brittle domain removal phase

$$V_{2a}(m) = l_2(m) h_{2a}^2 \tan \theta. \tag{29}$$

It is obtained from $V_2(m) = V_{2a}(m)$ as follows:

When $l_2(m) = l'_2(m)$, the average depth of cut $h_{2a}(m)$ in the bone meal removal phase can be obtained from the equation $V_2(m) = V_{2a}(m)$ as follows:

$$h_{2a}(m) = \sqrt{\frac{[l_1(m) + l_2(m)]h_2^2 - l_1(m)h_1^2}{3l_2(m)}}. \quad (30)$$

2.4.3 Brittle Domain Removal Phase

As shown in Figure 10(a), the material removal volume $V_3(m)$ of different layers of single diamond abrasive grain in the brittle domain removal stage, when $h_2 < h_{u3} < S$, can be determined using the following expression:

$$V_3(m) = \frac{1}{3}[l_1(m) + l_2(m) + l_3(m)]h_3^2 \tan \theta - \frac{1}{3}[l_1(m) + l_2(m)]h_2^2 \tan \theta. \quad (31)$$

The length of the trajectory of the brittle domain removal stage at time t_2-t_3 is $l_3(m)$. Assuming that the equivalent material removal volume of different layers of a single diamond abrasive grain is shaped as a triangular prism with the same cross-sectional area, as shown in Figure 10(b), the equivalent volume $V_{3a}(m)$ can be calculated as follows:

$$V_{3a}(m) = l_3(m)h_{3a}^2(m) \tan \theta, \quad (32)$$

when $l_3(m) = l'_3(m)$, the average depth of cut $h_{3a}(m)$ in the brittle domain removal phase can be obtained from the equation $V_3(m) = V_{3a}(m)$ as follows:

$$h_{3a}(m) = \sqrt{\frac{[l_1(m) + l_2(m) + l_3(m)]h_3^2 - [l_1(m) + l_2(m)]h_2^2}{3l_3(m)}}, \quad (33)$$

where $h_3 = S$.

3 Grinding Force Model

The predictive force model can reveal the transfer and reduction mechanism of biological bone micro-grinding force in different removal stages of bone material under ultrasonic vibration of a spherical grinding head. In accordance with the dynamic grinding behavior of biological bone tissue material removal under ultrasonic vibration-assisted micro-grinding in Section 2, the critical cutting depth was derived, and the relationship between grinding force and cutting depth of single diamond in different layers was given. The dynamic grinding force models of different removal stages were calculated in accordance with the different instantaneous interactions of effective abrasive particles in each layer. Finally, the grinding force prediction model of x , y , and z axes, which accords with the actual grinding direction of bone surgery, was obtained by calculus.

3.1 Grinding Forces at Different Removal Stages

3.1.1 Grinding Force Model for Ductile Removal Stage

The bone material is in the state of ductile domain removal, where the material removal primarily depends on the extrusion and shear effects between the abrasive and the workpiece, and microcracks rarely occur. The relationship between the cutting depth h_1 of a single diamond abrasive grain and the cutting force F_{n1} can be expressed as follows [52, 53]:

$$h_1 = \left(\frac{1}{2 \tan \theta \sqrt{\tan^2 \theta + 2}} \cdot \frac{F_{n1}}{H_v} \right)^{1/2}. \quad (34)$$

Therefore, from the above equation, the relationship between the average normal cutting force $F_{n1}(m)$ and the average depth of cut $h_{1a}(m)$ of different layers of single abrasive grains in the removal stage of the ductile domain can be expressed as follows:

$$F_{n1}(m) = 2H_{v_u}h_{1a}^2(m) \tan \theta \sqrt{(\tan^2 \theta + 2)}. \quad (35)$$

During the ductile domain removal stage, as the depth of cut is increased, the plastic deformation of the workpiece is initiated at the yield criterion point, and the friction force $F_{t1}(m)$ in the tangential direction mainly affects the different layers of single diamond particles, with the expression as follows:

$$F_{t1}(m) = \mu_1 F_{n1}(m), \quad (36)$$

where μ_1 is the coefficient of friction.

The friction coefficient of diamond particles can be approximated as the ratio of the projected area in the cutting and tangential directions [54], as illustrated below:

$$\mu_1 = \frac{S_{t1}(m)}{S_{n1}(m)}. \quad (37)$$

As shown in Figure 11, $S_{t1}(m)$ and $S_{n1}(m)$ are the tangential and normal projected areas of diamond particles in the removal stage of the ductile domain, respectively, which can be expressed as

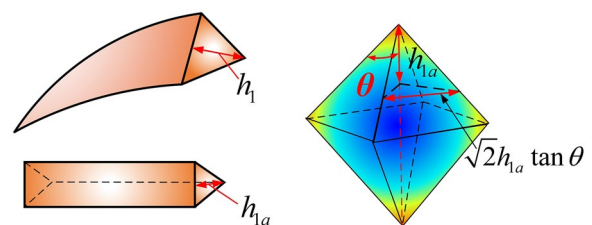


Figure 11 Tangential and normal projected areas of diamond particles in the removal stage of ductile domains

$$\begin{cases} S_{t1}(m) = \frac{1}{2} \cdot 2h_{1a}(m) \tan(\theta)h_{1a}(m) = h_{1a}^2(m) \tan \theta, \\ S_{n1}(m) = \left[\sqrt{2}h_{1a}(m) \tan(\theta) \right]^2 = 2h_{1a}^2(m) \tan^2 \theta. \end{cases} \quad (38)$$

As a result, the average tangential cutting force $F_{t1}(m)$ for various layers of single abrasive grains during the ductile domain removal stage can be expressed in the following manner:

$$F_{t1}(m) = H_{v-u}h_{1a}^2(m) \left(2 + \tan^2 \theta \right)^{1/2}. \quad (39)$$

3.1.2 Grinding Force Model for Bone Meal Removal Stage

As depicted in Figure 9, the equivalent removal volume V_{2a} of diamond particles can also be expressed in terms of the removal volume V_{2b} observed during the initial crack extension stage by the diamond abrasive grains and the mechanism of bone material removal, taking into account the interference effect as follows:

$$V_{2b}(m) = \frac{1}{2} \cdot 2 \cdot C_l(m) \cdot C_h(m) \cdot l_2(m) = C_2^2 \cdot \cot^{3/4} \theta \cdot \frac{E^{7/8}}{H_{v-u}^{3/2} \cdot K_{id}^{1/2} \cdot (1 - \nu^2)^{1/4}} \cdot F_{n2}^9 \cdot l_2(m), \quad (40)$$

where $C_l(m)$ is the lateral crack length, and $C_h(m)$ is the lateral crack depth, which can be obtained from Eqs. (46) and (47).

The average normal grinding forces for different layers of individual diamond abrasive grains at $V_{2b}(m) = V_{2a}(m)$ during the bone meal removal stage are as follows:

$$F_{n2}(m) = \left[\frac{h_{2a}^2(m) \cdot \tan \theta \cdot H_{v-u}^{3/2} \cdot K_{id}^{1/2} \cdot (1 - \nu^2)^{1/4}}{C_2^2 \cdot \cot^{3/4} \theta \cdot E^{7/8}} \right]^{8/9}. \quad (41)$$

The tangential force in the bone meal removal phase can be expressed as

$$F_{t2} = \sigma_s S_{t2}, \quad (42)$$

where σ_s is the compressive yield stress in the contact region [47], which is defined as follows:

$$\sigma_s = C \left(\frac{H_{v-u}^4}{E} \right)^{1/3}, \quad (43)$$

where C is a dimensionless constant, and it is 1.5 for hard and brittle materials [55].

Meanwhile, $S_{t2}(m)$ is the tangential projected area of the diamond particles with respect to the depth of cut, and it can be calculated from the average depth of cut as follows:

$$S_{t2}(m) = \frac{1}{2} \cdot 2 \cdot h_{2a}(m) \cdot \tan \theta \cdot h_{2a}(m) = h_{2a}^2(m) \cdot \tan \theta. \quad (44)$$

Thus, the average tangential grinding forces for different layers of individual diamond abrasive grains during the bone meal removal stage are as follows:

$$F_{t2}(m) = Ch_{2a}^2(m) \tan \theta \left(\frac{H_{v-u}^4}{E} \right)^{1/3}. \quad (45)$$

3.1.3 Grinding Force Model for Brittle Removal Stage

In the brittle zone, material removal is achieved through crack creation and expansion. As illustrated in Figure 10, medial-radial cracks and lateral cracks are formed below the abrasive grains. With the increase in load, the lateral cracks could propagate and eventu-

ally reach the workpiece surface. This process results in the formation of chips to remove the bone material. The lateral crack length ($C_l(m)$) and lateral crack depth ($C_h(m)$) can be determined using the following equations [39, 53]:

$$C_l(m) = C_2(\cot \theta)^{5/12} \cdot \left[\frac{E^{3/4}}{H_{v-u}K_{id}(1 - \nu^2)^{1/2}} \right]^{1/2} \cdot F_{nb}^{5/8}, \quad (46)$$

$$C_h(m) = C_2(\cot \theta)^{1/3} \cdot \frac{E^{1/2}}{H_{v-u}} \cdot F_{nb}^{1/2}, \quad (47)$$

where E is the Young's modulus of the workpiece material, MPa; K_{ic} is the static fracture toughness of the workpiece material, MPa·m^(1/2); ν is the Poisson's ratio of the workpiece material; F_{nb} is the load applied to the abrasive grains, N; C_2 is a dimensionless constant, independent of the material indentation system; and $C_2 = 0.226$ [56].

The average normal grinding forces $F_{n3}(m)$ and tangential grinding forces $F_{t3}(m)$ for different layers of individual diamond abrasive grains during the brittleness removal stage are as follows [54]:

$$F_{n3}(m) = \frac{1}{C_2} h_{3a}^2(m) H_{v_u}^2 \tan^{8/3} \theta \left[\frac{3(1-2\nu)}{E(5-4\nu)} + \frac{2\sqrt{3} \cot \theta}{\pi(5-4\nu)\sigma_s} \right], \quad (48)$$

$$F_{t3}(m) = \frac{C_l(m)}{C_2 C_h(m)} h_{3a}^2(m) H_{v_u}^2 \tan^{8/3} \theta \left[\frac{3(1-2\nu)}{E(5-4\nu)} + \frac{2\sqrt{3} \cot \theta}{\pi(5-4\nu)\sigma_s} \right]. \quad (49)$$

3.2 Effective Number of Abrasive Grains

3.2.1 Total Effective Number of Abrasive Grains

Computing the number of effective diamond abrasive grains, denoted as $V_m(m)$, in various layers during a single rotational cycle becomes essential to account for the variability in the height and distribution of the abrasive grain prominence. This calculation is crucial for obtaining the final average cutting force. The total theoretical removal volume, denoted as $V_s(m)$, over half a grinding rotational cycle was analyzed to simplify the process. This analysis depends on factors, such as the level of interference between the diamond and the workpiece during the ductile domain removal stage, the bone meal removal stage, and the extension of transverse cracks during the brittle domain removal stage. The mathematical expression for this analysis is as follows:

$$V_s(m) = l_1(m) h_{1a}^2(m) \tan \theta + l_2(m) h_{2a}^2(m) \tan \theta + 2l_3(m) C_h(m) C_l(m). \quad (50)$$

The total material removal volume $V_m(m)$ in half a rotation cycle can be expressed as follows:

$$V_m(m) = \frac{\pi R a_p S}{2}. \quad (51)$$

Therefore, the theoretical number of diamond particles in contact between the spherical grinding head and the workpiece during half a cycle of the grinding process is as follows:

$$N_m(m) = \frac{V_m(m)}{V_s(m)}. \quad (52)$$

3.2.2 Effective Number of Abrasive Grains in the Three Removal Stages

The effective number of abrasive grains in the $[0, \pi/2]$ region can be obtained first to facilitate the analysis, because the effective abrasive grains are symmetrically distributed in the $[0, \pi]$ region.

The effective number of abrasive grains in the $[0, \pi/2]$ region of ductile removal can be calculated as follows:

$$N_1(m) = N_m(m) \cdot \frac{2 \cdot R \cdot \varphi_1}{2 \cdot R \cdot \varphi_3}. \quad (53)$$

The effective number of abrasive grains in the $[0, \pi/2]$ region of bone meal removal can be obtained as follows:

$$N_2(m) = N_m(m) \cdot \frac{2 \cdot R \cdot (\varphi_2 - \varphi_1)}{2 \cdot R \cdot \varphi_3}. \quad (54)$$

The effective number of abrasive grains in the $[0, \pi/2]$ region of brittle fracture can be expressed as follows:

$$N_3(m) = N_m(m) \cdot \frac{2 \cdot R \cdot (\varphi_3 - \varphi_2)}{2 \cdot R \cdot \varphi_3}. \quad (55)$$

3.3 Dynamic Grinding Force Evolution Mechanism in Grinding Zone

3.3.1 Tangential and Normal Forces at Different Contact Stages

The normal and tangential forces in half a cycle should be analyzed first for ease of calculation, because the tangential and normal forces are symmetrically distributed in a motion cycle.

The total normal and tangential forces in the ductile removal phase during half a cycle are as follows:

$$\begin{cases} F_{n1_z}(m) = N_1(m) F_{n1}(m), \\ F_{t1_z}(m) = N_1(m) F_{t1}(m). \end{cases} \quad (56)$$

The total normal and tangential forces in the bone meal removal phase during half a cycle are as follows:

$$\begin{cases} F_{n2_z}(m) = N_2(m) F_{n2}(m), \\ F_{t2_z}(m) = N_2(m) F_{t2}(m). \end{cases} \quad (57)$$

The total normal and tangential forces in the brittle removal phase during half a cycle are as follows:

$$\begin{cases} F_{n3_z}(m) = N_3(m) F_{n3}(m), \\ F_{t3_z}(m) = N_3(m) F_{t3}(m). \end{cases} \quad (58)$$

3.3.2 Influence of Geometric Properties on Grinding Forces

As illustrated in Figure 12(a), the complete effective grinding zone can be identified as follows:

$$\varphi(t) = \frac{2\pi n}{60} t, \quad (59)$$

where $t \in [0, 60/n]$, so $\varphi(t) \in [0, \pi]$.

As depicted in Figure 12(c), the forces in x - and y -axes, which are generated by F_t within the effective grinding zone of the spherical grinding head, can be described as follows:

$$F_{x1} = F_t \cdot \cos[\varphi(t)]. \quad (60)$$

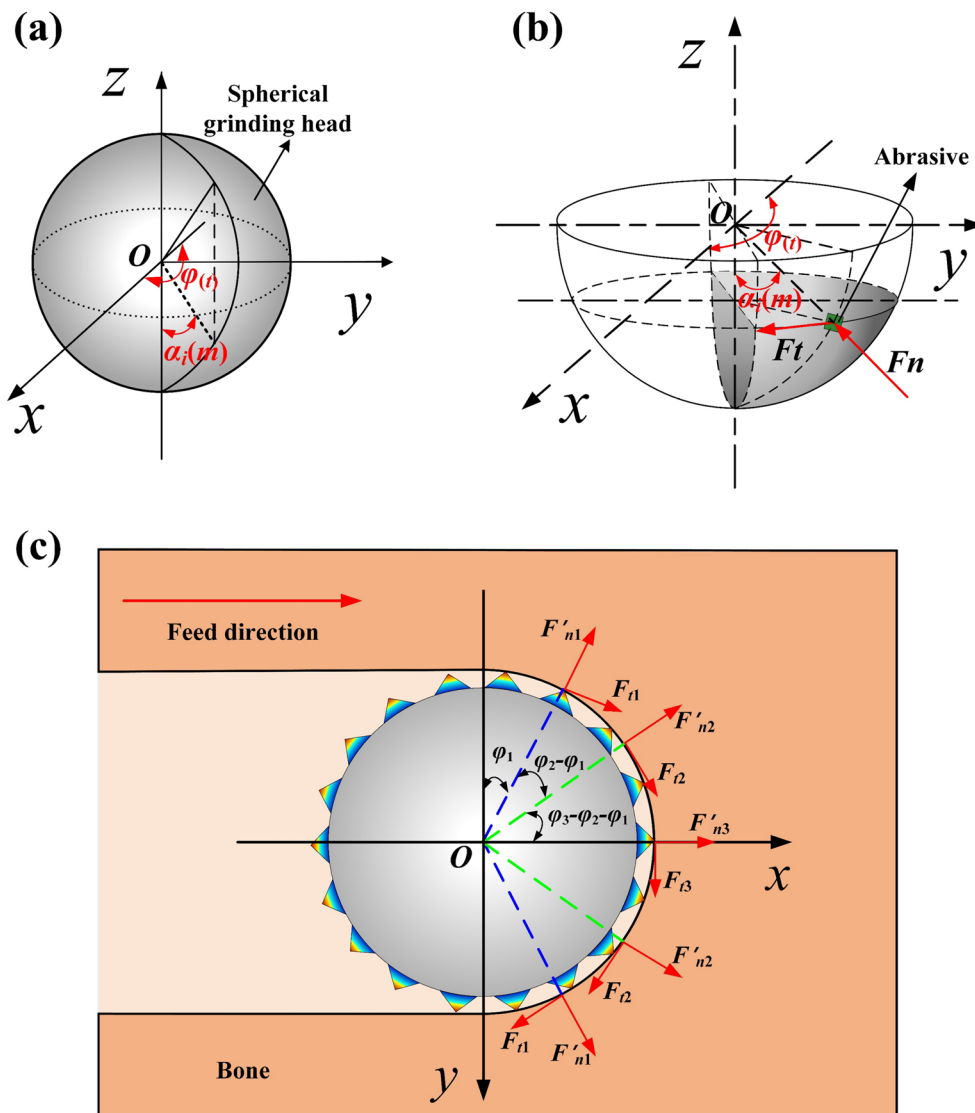


Figure 12 Three-dimensional spatial force analysis of spherical grinding head

The F_{x1} produced by F_t in $\varphi \in [0, \pi/2]$ and F_t in $\varphi \in [\pi/2, \pi]$ cancel each other out, so $F_{x1} = 0$ in the effective grinding zone.

$$F_{y1} = F_t \cdot \sin[\varphi(t)]. \tag{61}$$

The forces in x - and y -axis generated in the effective grinding zone F_n of the spherical grinding head are:

$$F'_n = F_n \cdot \sin[\alpha_i(m)], \tag{62}$$

where F'_n is the component force of F_n in the direction of the horizontal plane in three dimensions, as shown in Figure 12(b).

As shown in Figure 12(c), the fractional force of F'_n at each of the three removal stages can be expressed as follows:

$$\begin{cases} F'_{n1} = F_{n1} \cdot \sin[\alpha_i(m)], \\ F'_{n2} = F_{n2} \cdot \sin[\alpha_i(m)], \\ F'_{n3} = F_{n3} \cdot \sin[\alpha_i(m)]. \end{cases} \tag{63}$$

The forces on the x - and y -axes generated by F'_n are as follows:

$$F_{x2} = F'_n \cdot \sin[\varphi(t)] = F_n \cdot \sin[\alpha_i(m)] \cdot \sin[\varphi(t)], \tag{64}$$

$$F_{y2} = F'_n \cdot \cos [\varphi(t)] = F_n \cdot \sin [\alpha_i(m)] \cdot \cos [\varphi(t)]. \tag{65}$$

The F_{y2} produced by F'_n in $\varphi \in [0, \pi/2]$ and the F'_n in $\varphi \in [\pi/2, \pi]$ cancel each other out, so $F_{y2} = 0$ in the effective grinding zone.

So, the force in x - and y -axes directions for a single layer of effective abrasive grains can be obtained as follows:

$$F'_x = F_{x2}, \tag{66}$$

$$F'_y = F_{y1}. \tag{67}$$

3.3.3 x -Direction Grinding Force Model

On the basis of the above analysis, the x -direction grinding force model can be derived.

$$F_{x2_2}(m) = \int_{\varphi_1}^{\varphi_2} F_{n2_z}(m) \sin [\alpha_i(m)] \sin [\varphi(t)] dt. \tag{69}$$

The forces in x -axis direction for different layers of the effective abrasive grain brittleness removal stage during half a grinding cycle are as follows:

$$F_{x2_3}(m) = \int_{\varphi_2}^{\varphi_3} F_{n3_z}(m) \sin [\alpha_i(m)] \sin [\varphi(t)] dt. \tag{70}$$

The grinding forces in x -axis direction for different layers of single abrasive grains in one grinding cycle are as follows:

$$F_x(m) = F_{x2}(m) = 2[F_{x2_1}(m) + F_{x2_2}(m) + F_{x2_3}(m)]. \tag{71}$$

The total grinding force in x -axis direction in the effective grinding zone is as follows:

$$F_x = 2 \sum_{m=1}^{L_c} N_m(m) \frac{\sin [\alpha_i(m)]}{\varphi_3} \left\{ \begin{aligned} & \left[\frac{\varphi_1 H_{v_u} h_2^2 \tan \theta (\tan^2 \theta + 2)^{1/2} \int_0^{\varphi_1} \sin [\varphi(t)] dt}{24} + \right. \\ & \left. \frac{(\varphi_2 - \varphi_1) \int_{\varphi_1}^{\varphi_2} \sin [\varphi(t)] dt h_2^{16/9} [15l_1(m) + 16l_2(m)]^{8/9} \tan^{14/9} \theta H_{v_u}^{4/3} K_{id}^{4/9} (1 - \nu^2)^{2/9}}{(0.226^{16/9}) [48l_2(m)]^{8/9} E^{7/9}} + \right. \\ & \left. \frac{(\varphi_3 - \varphi_2) \int_{\varphi_2}^{\varphi_3} \sin [\varphi(t)] dt}{0.678} \cdot \frac{S^2 l_{c_ui}(m) - h_2^2 [l_1(m) + l_2(m)]}{l_3(m)} \cdot \frac{H_{v_u}^2 \tan^{8/3} \theta}{5 - 4\nu} \right. \\ & \left. \left[\frac{3(1 - 2\nu)}{E} + \frac{4\sqrt{3} \cot \theta}{3\pi} \left(\frac{E}{H_{v_u}^4} \right)^{1/3} \right] \right\}. \tag{72}$$

The forces in x -axis direction for the different layers of the effective abrasive grain ductile removal stage during half a grinding cycle are as follows:

$$F_{x2_1}(m) = \int_0^{\varphi_1} F_{n1_z}(m) \sin [\alpha_i(m)] \sin [\varphi(t)] dt. \tag{68}$$

The forces in x -axis direction for the different layers of effective abrasive bone meal removal stages during half a grinding cycle are as follows:

3.3.4 y -Direction Grinding Force Model

On the basis of the above analysis, the y -direction grinding force model can be derived.

The forces in y -axis direction for the different layers of the effective abrasive grain ductile removal stage during half a grinding cycle are as follows:

$$F_{y1_1}(m) = \int_0^{\varphi_1} F_{t1_z}(m) \sin [\varphi(t)] dt. \tag{73}$$

The forces in y -axis direction for the different layers of effective abrasive bone meal removal stages during half a grinding cycle are as follows:

$$F_{y1_2}(m) = \int_{\varphi_1}^{\varphi_2} F_{t2_z}(m) \sin [\varphi(t)] dt. \tag{74}$$

The forces in y -axis direction for different layers of the effective abrasive grain brittleness removal stage during half a grinding cycle are as follows:

$$F_{y1_3}(m) = \int_{\varphi_2}^{\varphi_3} F_{t3_z}(m) \sin [\varphi(t)] dt. \tag{75}$$

The grinding forces in y -axis direction for different layers of individual abrasive grains in a single grinding cycle are as follows:

3.3.5 z-Direction Grinding Force Model

On the basis of the above analysis, the z -direction grinding force model can be derived.

The grinding forces in z -axis direction for different layers of single abrasive grain in one grinding cycle are as follows:

$$F_z(m) = 2 \{ F_{n1_z}(m) \cos [\alpha_i(m)] + F_{n2_z}(m) \cos [\alpha_i(m)] + F_{n3_z}(m) \cos [\alpha_i(m)] \}. \tag{78}$$

The total grinding force in z -axis direction in the effective grinding zone is as follows:

$$F_z = 2 \sum_{m=1}^{L_e} \frac{N_m(m)}{\varphi_3} \left\{ \begin{aligned} & \frac{\varphi_1 H_{v_u} h_2^2 \tan \theta (\tan^2 \theta + 2)^{1/2} \cos [\alpha_i(m)]}{24} + \\ & \frac{(\varphi_2 - \varphi_1) \cos [\alpha_i(m)] h_2^{16/9} [15l_1(m) + 16l_2(m)]^{8/9} \tan^{14/9} \theta H_{v_u}^{4/3} K_{id}^{4/9} (1 - \nu^2)^{2/9}}{(0.226^{16/9}) [48l_2(m)]^{8/9} E^{7/9}} + \\ & \frac{(\varphi_3 - \varphi_2) \cos [\alpha_i(m)] \cdot S^2 l_{c_ui}(m) - h_2^2 [l_1(m) + l_2(m)] \cdot H_{v_u}^2 \tan^{8/3} \theta}{0.678 \cdot l_3(m) \cdot (5 - 4\nu)} \cdot \\ & \left[\frac{3(1 - 2\nu)}{E} + \frac{4\sqrt{3} \cot \theta}{3\pi} \left(\frac{E}{H_{v_u}^4} \right)^{1/3} \right] \end{aligned} \right\}. \tag{79}$$

$$F_y(m) = 2F_{y1}(m) = 2[F_{y1_1}(m) + F_{y1_2}(m) + F_{y1_3}(m)]. \tag{76}$$

The total grinding force in y -axis direction in the effective grinding zone is as follows:

4 Experimental Verification

Ultrasonic-assisted micro-grinding experiments were carried out on a bovine femur with a spherical grinding head under different machining parameters to verify the

$$F_y = 2 \sum_{m=1}^{L_e} \frac{N_m(m)}{\varphi_3} \left\{ \begin{aligned} & \frac{\varphi_1 H_{v_u} h_2^2 (\tan^2 \theta + 2)^{1/2} \int_0^{\varphi_1} \sin [\varphi(t)] dt}{48} + \\ & \frac{(\varphi_2 - \varphi_1) h_2^2 \int_{\varphi_1}^{\varphi_2} \sin [\varphi(t)] dt [15l_1(m) + 16l_2(m)] \tan \theta H_{v_u}^{4/3}}{32l_2(m) E^{1/3}} + \\ & \frac{(\varphi_3 - \varphi_2) \int_{\varphi_2}^{\varphi_3} \sin [\varphi(t)] dt \cdot S^2 l_{c_ui}(m) - h_2^2 [l_1(m) + l_2(m)] \cdot C_l(m) \cdot H_{v_u}^2 \tan^{8/3} \theta}{0.678 \cdot l_3(m) \cdot C_h(m) \cdot (5 - 4\nu)} \cdot \\ & \left[\frac{3(1 - 2\nu)}{E} + \frac{4\sqrt{3} \cot \theta}{3\pi} \left(\frac{E}{H_{v_u}^4} \right)^{1/3} \right] \end{aligned} \right\}. \tag{77}$$

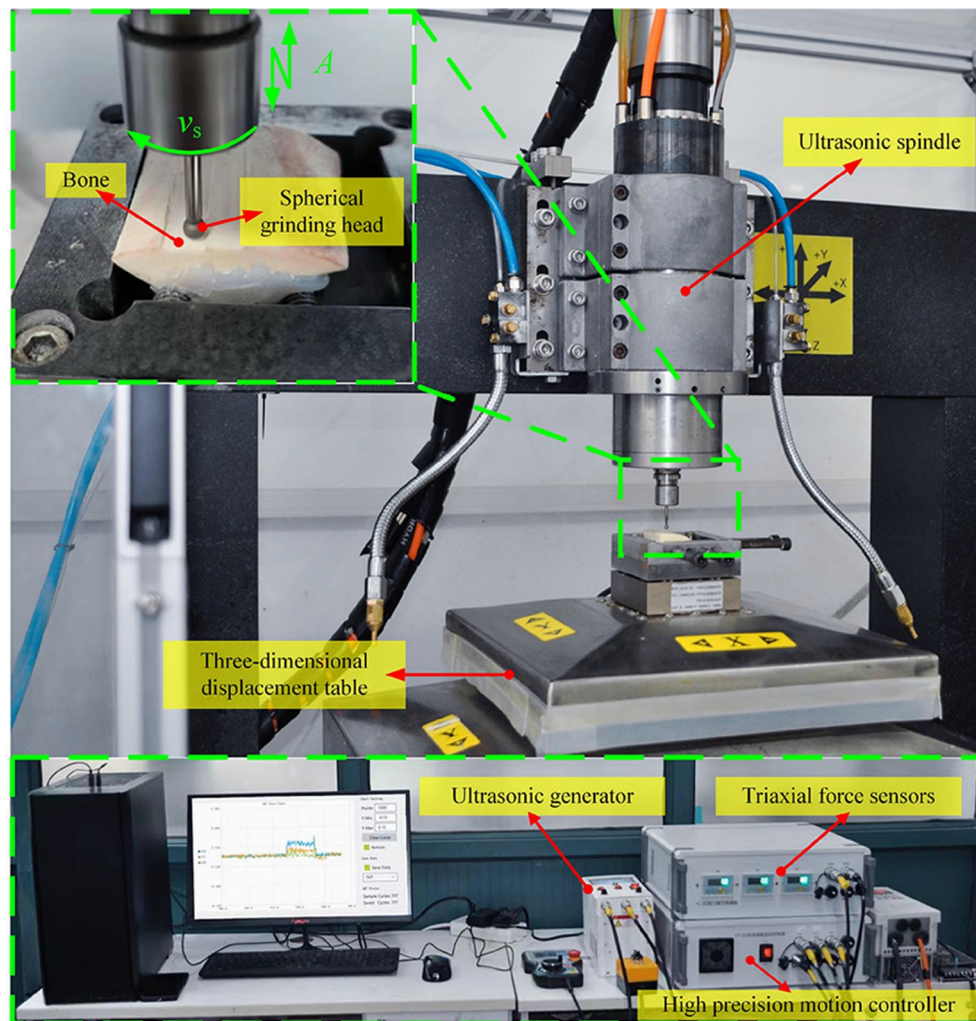


Figure 13 Experimental material and equipment

feasibility and accuracy of the above numerical calculation method.

4.1 Experimental Equipment

A 3D grinding force dynamometer (YDM-III99, Dalian University of Technology, China) was used for real-time continuous measurement of the grinding force in x -, y -, and z -axis directions, as shown in Figure 13. The dynamometer was connected to the charge amplifier via high-transmittance leads, and the A/D data acquisition card installed on the PC facilitated data collection. Dyno Ware software was utilized to measure and record the grinding force. A sampling frequency of 1 kHz was chosen on the basis of equipment performance and previous laboratory work [56, 57], ensuring optimal capture of grinding force information. Furthermore, Dyno Ware's low-pass filtering was utilized to denoise the acquired grinding force signal. For the grinding force analysis, 100

data points were carefully selected around the center of the effective grinding area as the benchmark. The average value was then calculated to determine the corresponding force average value. During the experiment, the bone unit was placed horizontally along the direction parallel to the x -axis.

4.2 Experimental Materials

4.2.1 Handling of Bone Material

In this experiment, the test material consisted of dense bone sourced from fresh bovine femur, chosen due to its mechanical properties being most similar to human bone [57]. All bones were obtained from 2–3-year-old adult cattle weighing approximately 500 kg to minimize the effect of factors, such as gender and age, on the results and to reduce differences between biological individuals. The cylindrical bone stems, which exhibited relatively uniform diameter and size, were extracted and

subsequently had their bone marrow removed. These cylindrical bone stems were then cut into blocks by using an angle grinder. An ultrasonic-vibration-assisted micro-grinding device with a mounted 120# cylindrical grinding head was utilized for processing the bone surface to achieve a smooth surface, particularly in the area targeted for grinding. The resulting bone samples featured dimensions of 40 mm × 20 mm × 5 mm. The samples underwent further polishing with sandpaper to eliminate any potential damage incurred during sample preparation, ensuring a flat and smooth surface for processing. Subsequently, the samples were treated with saline solution. While some samples underwent immediate experimentation, others were stored in a freezer at - 20 °C to preserve their thermophysical properties and moisture

for subsequent experiments [33]. However, all specimens were limited to a maximum storage duration of 1 week to prevent any alterations in tissue properties arising from prolonged storage to ensure comparability of the experimental results. Removing the bone blocks from the freezer and allowing them to reach room temperature for 1 hour before each experiment were crucial to allow the bone samples to regain their biological properties during the experiments.

4.3 Experimental Design

4.3.1 Experimental Condition

The experiments were conducted in the operating room maintained at a temperature of 20 °C to ensure the bone samples were in optimal state for testing and analysis.

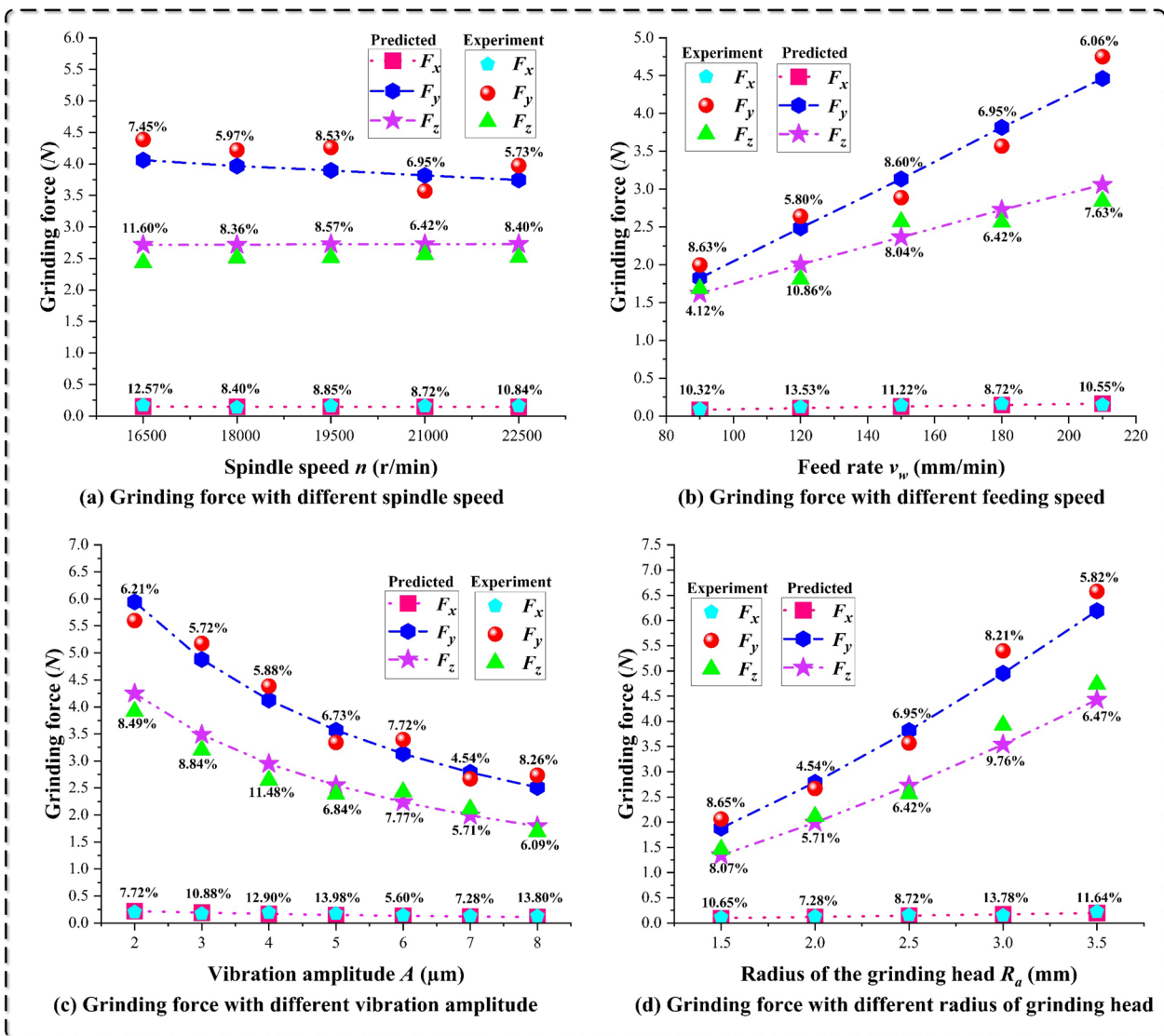


Figure 14 Comparison of experimental and theoretical values of grinding force under different process parameters

Given the hard and brittle nature of biological bone, the 120# electroplated diamond spherical grinding head, known for its stable processing quality and excellent overall performance, was chosen. The grinding head had a diameter ranging from 3 mm to 7 mm and a shank diameter of 3 mm. The bone tissue composition includes certain polysaccharide proteins [58]. When the grinding temperature increases, the viscosity of these polysaccharide proteins in the grinding chips also increases. Additionally, due to the extrusion between the abrasive tool and the bone surface, the debris adheres to the surface of the abrasive tool, leading to potential clogging issues. A new abrasive tool was used for each set of data obtained to ensure the accuracy of the test data. This precaution was taken to prevent any contamination or inaccuracies caused by debris buildup on the grinding tool during consecutive tests.

4.3.2 Grinding Parameters

Its main technical parameters are as follows: spindle power of 2.5 kW, maximum speed (n) of 24000 r/min, vibration amplitude A of 2–8 μm , and frequency (f) of 18–22 kHz. Rotational speed is the frequency displayed by the frequency converter $\times 30$. For example, if the displayed frequency is 600, then the rotational speed is 18000 r/min. The x , y -axis multiplication of the three-dimensional table default unit is mm. The default unit of the z -axis multiplication of speed is nm. Multiple gradients were set for each parameter of the experiment, as shown in Table 1. Each experiment was repeated five times to minimize errors.

4.3.3 Mechanical Properties of Bone Materials

The study of the mechanical properties of bone tissue can provide important theoretical basis for bone surgery and has important significance for improving the effect of bone surgery. The mechanical properties of bovine femur are shown in Table 2.

5 Numerical Analysis

5.1 Assessment of the Model

Figure 14 displays the accuracy analysis of the predicted and experimental values of the grinding force concerning the input variables. The established x -axis, y -axis, and z -axis grinding force models were employed to predict the grinding force under various input variables. This approach helps to gain deeper insights into the factors influencing the grinding force of the spherical grinding head on bone, particularly when subjected to ultrasonic vibration.

Figure 14(a) illustrates the impact of spindle speed on the grinding force. While keeping the grinding width, feed rate, and amplitude constant, the grinding force

diminishes as the spindle speed increases. This phenomenon can be attributed to several factors. First, as the spindle speed increases, a larger number of diamond particles participate in the grinding process when a certain volume of material is displaced. Consequently, the grinding time is shortened, and the contact depth of diamond particles with the workpiece decreases. Moreover, the maximum undeformed chip thickness of individual diamond grains reduces, leading to lower material removal in brittle regions, thus reducing the cutting force per grain. Higher cutting speeds decrease the likelihood of continuous crack opening, increase fracture density flow toughness, and reduce strength degradation. As a result, the final grinding force decreases, aligning with the trend observed in the experimental results.

Figure 14(b) depicts the influence of the feed rate on the cutting force. While keeping the spindle speed, grinding width, and amplitude constant, the cutting force evidently increases with an increase in feed rate. This observation aligns with the experimental results, as lower feed rates involve a higher number of diamond particles in the grinding process, leading to a shallower depth of engagement between the diamond particles and the workpiece. This localized stress concentration causes cracks to gradually form and expand from the second stage. Once the cracks are formed and extended, the tensile stress concentration diminishes, and no further crack nucleation occurs until the next tensile stress concentration is established. As a consequence, at low feed rates, tensile stresses continuously accumulate in the workpiece, resulting in a high likelihood of continuous cracking and crack interaction. The reduced material removal rate leads to a decrease in the thickness of undeformed chips, promoting more plastic flow and less brittle fracture, subsequently resulting in reduced cutting forces.

Figure 14(c) illustrates the impact of the amplitude value on the cutting force. With the spindle speed

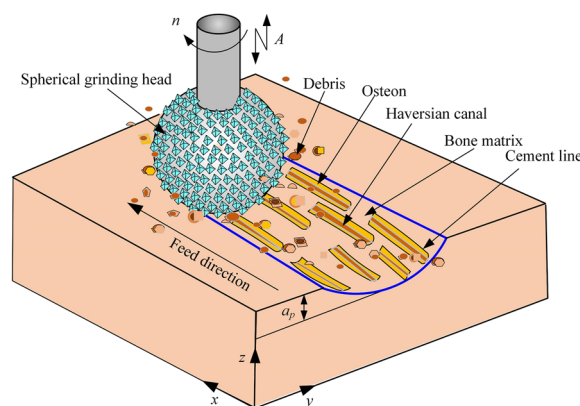


Figure 15 Schematic of the grinding force reduction mechanism

and grinding width kept constant, the grinding force decreases as the amplitude increases, because as the amplitude increases, the motion contact arc length increases, and the maximum undeformed chip thickness decreases, thus increasing the range of ductile removal and bone meal removal. At the same time, ultrasonic vibration has a weakening effect on the bone surface hardness and fracture toughness causing softening of the workpiece, which also promotes the reduction in grinding force.

Figure 14(d) depicts the influence of the radius of the grinding head (grinding width) on the cutting force. With the spindle speed and feed rate maintained constant, the cutting force evidently increase with an increase in grinding width. This effect can be attributed to the enlargement of the contact area between the tool and the workpiece when the cutting width is increased, resulting in more diamond particles participating in the grinding process. The greater cutting forces may cause partial deformation of the tool, leading to a longer actual contact length than the theoretical one. Furthermore, as the width of cut increases, the percentage of brittle areas cut also increases, which further amplifies the grinding force. Therefore, considering the effect of grinding width on the cutting force during experimental design and analysis is important.

Figure 14 clearly shows that the force in y direction is greater than the force in z direction and is significantly greater than the force in x direction, and the force in the y axis increases and decreases faster than the force in z axis. This difference is related not only to the geometric features and movement rules of spherical grinding head but also to the structural characteristics of bone tissue [49, 65, 66]. During the experiment, the bone unit is positioned horizontally along the feeding direction (x -axis), and within the dense bone, cylindrical bone units are distributed along the axial direction, as shown in Figure 15. When the force is applied along the x -axis, the bone units are more likely to fracture obliquely, with their strength predominantly determined by the bone units. Consequently, the compressive strength of the x -axis direction of the bone tissue is the lowest. When the force is applied along the y -axis and z -axis directions, the compressive load acts perpendicular to the bone unit within the bone tissue, subjecting the bone unit to extrusion. Under compression along the y -axis, the inner and outer ring bone plates, and the inter-bone plate, bear the support load. When the load reaches a critical level, the bone plates tend to fracture and lose their load-bearing capacity, subsequently transferring the load primarily to the bone unit. As the squeezing force on the bone units increases, they fracture in contact with one another, leading to a decrease in compressive strength in y -axis

direction under the influence of ultrasonic vibration. In z -axis direction, the bone plate and the bone unit experience extrusion without any fracture, and only when a sufficiently high stress is applied, the circular bone plate of the bone unit undergoes pressing and breaking. Due to the small size of the bone unit at approximately 200–400 μm [49], the compressive strength of the bone tissue in z -axis direction is exceptionally high. Meanwhile, the force in y -axis direction increases more rapidly than the force in z -axis direction with an increase in the feed rate, because the effective contact surface of the spherical grinding head is a rounded surface (Figure 14(b)). Additionally, the force in y -axis direction decreases more quickly than the force in z -axis direction with an increase in amplitude under the effect of ultrasonic vibration (Figure 14(c)). Lastly, the force in y -axis direction increases more swiftly than the force in z -axis direction with an increase in grinding width (Figure 14(d)).

Bone material is anisotropic, and this analytical model involves idealization and computational properties of bone material. In this study, appropriate idealization of bone material was performed, and the mechanism and force model for removing biological bone material were established using a spherical grinding head assisted by ultrasonic vibration. In addition, during the actual grinding process, the diamond particles may show some abrasion, resulting in some deviations. As shown in Figure 14, the maximum error of the theoretical value of the force in the direction of x -axis compared with the experimental value is 13.98%, and the minimum error is 5.60%; the maximum error of the theoretical value of the force in the direction of y -axis compared with the experimental value is 8.65%, and the minimum error is 5.60%; and the maximum error of the theoretical value of the force in the direction of z -axis compared with the experimental value is 11.60%, and the minimum error is 4.12%.

The findings indicate that UVAG with a spherical grinding head is an effective approach for bone grinding, leading to a reduction in grinding force. The model revealed that higher spindle speeds, lower feed rates, larger amplitudes, and smaller grinding widths contributed to lower cutting forces. Furthermore, feed rate, amplitude, and grinding width exerted a more significant effect on cutting forces than spindle speed. The developed model enables accurate assessment of force magnitude during bone material machining, prediction of crack length, and effective enhancement of machining efficiency while ensuring machining quality.

5.2 Effect of Bone Tissue on Grinding Forces

Based on the aforementioned model, the removal mode during bone material removal using UVAG with a spherical grinding head comprises a mixture of ductile domain

removal, bone powder removal, and brittle domain removal. Bone material, composed mainly of bone units and bone matrix, bears a structural resemblance to fiber-reinforced composite materials, with the bone unit fibers acting as reinforcement, contributing to its anisotropic mechanical properties [25, 67, 68].

The observed fluctuations in the cutting force during the grinding process are attributed to the spherical grinding head passing through the bone unit fibers, which are stronger than the matrix, as demonstrated in Figure 15. This phenomenon generates oscillatory fluctuations, and the frequency of these fluctuations is comparable to the size of the diameter of the bone unit. Meanwhile, the brittle fracture mode is characterized by the fracture of the bone unit fibers and the expansion of cracks, contributing to the dynamics of the grinding force in y -axis and z -axis directions. The amplitude of oscillatory fluctuations in the cutting force is associated with the generation of shear fractures and crack expansion on the shear surface. These phenomena indicate that the generation and expansion of cutting fractures in this mode cause significant fluctuations in the instantaneous value of the cutting force. According to the simulation results of Eqs. (46) and (47), the length of the cracks can be controlled within 100 μm [12–14]. This finding suggests that bone grinding in the ultrasonic vibratory micro-grinding mode can achieve self-repairing of the bone, meeting clinical requirements and avoiding bone damage that may occur during surgery due to excessive force. The cracks produced within the above experimental processing parameters fall within the range of human bone's self-repair capabilities, thereby reinforcing the suitability of the ultrasonic vibratory micro-grinding approach for bone material processing and highlighting its potential benefits in medical applications. This study presents valuable insights into the optimization of bone grinding processes, offering potential benefits in medical applications and bone-related industries.

6 Conclusions

The novel feature of this study is that it established a surface morphology model of spherical grinding head on the basis of the geometric characteristics of diamond grinding grains, revealed the gradual rule of contact arc length in accordance with the kinematic analysis of different grinding layers, and proposed a new method for calculating the maximum undeformed chip thickness of spherical grinding head assisted by ultrasonic vibration. The removal mechanism of biological bone tissue materials by ultrasonic vibration assisted micro-grinding was revealed. In accordance with the motion laws of ductile domain, bone meal, and brittle domain removals, a new ultrasonic vibration-assisted micro-grinding force

prediction model was established for spherical grinding head, and the mechanism of mechanical stress reduction was revealed. The conclusions of this study are as follows:

- (1) Different from previous studies on the contact arc length of spherical grinding head, the gradual contact arc length proposed in this study comprehensively considers the influence of geometric parameters and motion parameters. On the basis of the geometric characteristics of spherical grinding head, the influence of ultrasonic vibration, and the gradual rule of contact arc length, the dynamic transient changes in the maximum thickness of undeformed chips with the rotation radius R_i (m), the amplitude A , the spindle speed n , and the feed speed v_w were revealed. Matlab numerical simulation results show that with the increase in amplitude, the contact arc length of different layers increases, and the maximum thickness of undeformed chips decreases. The larger the amplitude is, the more uniform the change of the contact arc length and the maximum undeformed chip thickness from the bottom to the undeformed surface under ultrasonic vibration. Meanwhile, the smaller the amplitude is, the more obvious the gradient difference between the contact arc length and the maximum undeformed chip thickness from the bottom to the undeformed surface under ultrasonic vibration.
- (2) Ultrasonic vibration can not only reduce the maximum thickness of undeformed chips but also weaken the hardness and fracture toughness of the bone material, so it is easier to achieve the removal of the toughness domain of the bone material and the removal of bone powder, thereby reducing the grinding force. Under different process parameters, analysis of the geometric characteristics, movement laws, and bone structure characteristics of the spherical grinding head revealed that the micro-grinding force in y -axis direction is the largest, the micro-grinding force in x -axis direction is the smallest. Moreover, the reason why the micro-grinding force in y -axis direction increases and decreases faster than that in z -axis direction under the action of ultrasonic vibration was elucidated. Higher spindle speed, lower feed speed, larger amplitude, and smaller grinding width help reduce grinding forces. In addition, feed speed, amplitude, and grinding width have more influence on the micro-grinding force than spindle speed.
- (3) The numerical simulation value of Matlab is in good agreement with the experimental value. The results show that the average absolute errors of the predicted grinding force in x -axis direction are 9.88%,

10.87%, 10.31%, and 10.42%. The average absolute errors of grinding force prediction in y -axis direction are 6.93%, 7.21%, 6.44%, and 6.83%, and those of grinding force prediction in z -axis direction are 8.67%, 7.41%, 7.89%, and 7.28%. The maximum error of the x -axis force is 13.98%, and the minimum error is 5.60%. The maximum error of the y -axis force is 8.65%, and the minimum error is 5.60%. The maximum error of the z -axis force is 11.60%, and the minimum error is 4.12%. Therefore, the grinding force prediction model can effectively predict the micro-grinding force of biological bone.

Acknowledgements

Not applicable.

Author contributions

CL was responsible for the theoretical guidance, and JS wrote the manuscript. YZ, MY, TG, ML, XC, and BL provided some suggestions on the arrangement of the structure diagram and table in the paper. They also sorted out the relevant references. RL put forward some suggestions on the contents of the paper. DYS and SS read and approved the final manuscript. All authors read and approved the final manuscript.

Authors' Information

Jingang Sun, born in 1996, is a master of mechanical engineering majoring in *Qingdao University of Technology, China*. His current research interests focus on intelligent and clean precision grinding.

Changhe Li, born in 1966, is a professor of *Qingdao University of Technology, China*. He is a special expert of Taishan Scholars in Shandong Province, China. He received his Ph.D. degree from *Northeastern University, China*. His current research interests focus on intelligent and clean precision manufacturing. He has published 247 SCI/EI papers and won the China Patent Excellence Award (2 items) and Shandong Province Technical Invention 1st Prize.

Zongming Zhou, born in 1981, is graduated from *Beihang University, China*. The major is Information Engineering. He is currently a Chairman of Hanergy (Qingdao) Lubrication Technology Co., Ltd.

Bo Liu, born in 1984, is graduated from *Southwest University of Science and Technology, China*, majoring in mechanical design, manufacturing and automation. He is currently the Deputy General Manager of Sichuan Future Aerospace Industry LLC. His research interests include MQL complete set of technology, intelligent device and demonstration application.

Yanbin Zhang, born in 1990, is a professor of *Qingdao University of Technology, China*. He is a Xiangjiang Scholar from *The Hong Kong Polytechnic University, China*. He received his Ph.D. degree from *Qingdao University of Technology, China*. His current research interests focus on intelligent and clean precision manufacturing. He has published 35 papers, including in *International Journal of Machine Tools and Manufacture* and *Journal of Materials Processing Technology*. Among them, one is ESI hot paper, and three are ESI highly cited papers.

Min Yang, born in 1990, is graduated from *Qingdao University of Technology, China*, with research interests in intelligent and clean precision manufacturing. Her has presided over and participated in many national and provincial natural science funds and key R&D programs. Her has published more than 30 high-level papers in top journals and important international academic conferences at home and abroad; authorized 3 international patents such as the USA and 5 national invention patents; registered 4 software copyrights. Teng Gao, born in 1993, is a doctor of *Qingdao University of Technology, China*. His current research interests focus on intelligent and clean precision grinding. Mingzheng Liu, born in 1989, is a associate-professor of *Qingdao University of Technology, China*. He received his Ph.D. degree from *Qingdao University of Technology, China*. His current research interests focus on intelligent and clean precision grinding.

Xin Cui, born in 1990, is a associate-professor of *Qingdao University of Technology, China*. She received his Ph.D. degree from *Qingdao University of Technology, China*. Her current research interests focus on intelligent and clean precision grinding.

Benkai Li, born in 1991, is a lecturer of *Qingdao University of Technology, China*. He received his Ph.D. degree from *Nanjing University of Aeronautics and Astronautics, China*. His current research interests focus on intelligent and clean precision manufacturing of difficult-to-cut material.

Runze Li, born in 1993, received his B.S. degree in *Biomedical Engineering from Huazhong University of Science and Technology, China*, and M.S. degree in *Biomedical Engineering from University of Southern California, Los Angeles, CA*, in 2017. He received his Ph.D. degree at the *Department of Biomedical Engineering of University of Southern California, USA*. His research interests include development of high frequency transducer, ultrasonic elastography and optical coherence elastography.

Yusuf Suleiman Dambatta, born in 1989, received his Ph.D. degree from *University of Malaya, Malaya*. His current research interests focus on Manufacturing and precision machining.

Shubham Sharma is a senior lecturer in the *Department of Mechanical Engineering, IK Gujral Punjab Technical University, India*. His current research interests focus on advances in mechanical engineering, industrial and production engineering, manufacturing technology, advanced materials science and various characterizations.

Funding

Supported by National Natural Science Foundation of China (Grant Nos. 51975305, 52105457, and 52205481), the Special Fund of Taishan Scholars Project (Grant No. tsqn202211179), Shandong Provincial Youth Talent Promotion Project (Grant No. SDAST2021qt12), and Shandong Provincial Natural Science Foundation (Grant Nos. ZR2023QE057, ZR2022QE028, ZR2021QE116, and ZR2020KE027).

Availability of Data and Materials

The datasets supporting the conclusions of this article are included within the article.

Declarations

Ethics Approval and Consent to Participate

We declare that the papers we submitted are my research work under the guidance of the instructor and research results we have obtained. We confirm that this article has not been published previously and is not being submitted for publication elsewhere. We have not considered elsewhere except Chinese Journal of Mechanical Engineering. We confirm that this article has had the full consent of all authors. If this article was accepted, we confirm that it will not be published elsewhere in the same form, in English or in any other language, without the written consent of the publisher. The authors declare that they participated in this paper willingly.

Consent for Publication

The authors declare to consent to the publication of this paper.

Competing Interests

The authors declare no competing financial interests.

Author Details

¹School of Mechanical and Automotive Engineering, Qingdao University of Technology, Qingdao 266520, China. ²Hanergy (Qingdao) Lubrication Technology Co., Ltd., Qingdao 266520, China. ³Sichuan Future Aerospace Industry LLC., Shifang 618400, China. ⁴Department of Biomedical Engineering, University of Southern California, Los Angeles, CA 90089, USA. ⁵Mechanical Engineering Department, Ahmadu Bello University, Zaria 810106, Nigeria. ⁶Department of Mechanical Engineering and Advanced Materials Science, Regional Center for Extension and Development, Council of Scientific and Industrial Research (CSIR)-Central Leather Research Institute (CLR), Jalandhar 144021, India.

Received: 10 August 2023 Revised: 20 September 2023 Accepted: 22 September 2023
Published online: 27 October 2023

References

- [1] A Saraswathula, J L Porras, D Mukherjee, et al. Quality of life considerations in endoscopic endonasal management of anterior cranial base tumors. *Cancers*, 2023, 15(1): 195 <https://doi.org/10.3390/cancers15010195>.
- [2] I Zaed, A Cardia, R Stefani. From reparative surgery to regenerative surgery: state of the art of porous hydroxyapatite in cranioplasty. *International Journal of Molecular Sciences*, 2022, 23(10): 5434 <https://doi.org/10.3390/ijms23105434>.
- [3] A Pratap, K Patra, A A Dyakonov. A comprehensive review of micro-grinding: performance analysis, modeling techniques, and future research directions. *International Journal of Advanced Manufacturing Technology*, 2019, 104(1-4): 63-102. <https://doi.org/10.1007/s00170-019-03831-x>.
- [4] A J Shih, B L Tai, L H Zhang, et al. Prediction of bone grinding temperature in skull base neurosurgery. *Cirp Annals-Manufacturing Technology*, 2012, 61(1): 307-310. <https://doi.org/10.1016/j.cirp.2012.03.078>.
- [5] A Kabiri, M R Talaei. Non-Fourier bioheat model for bone grinding with application to skull base neurosurgery. *Proceedings of the Institution of Mechanical Engineers Part H-Journal of Engineering in Medicine*, 2022, 236(1): 84-93. <https://doi.org/10.1177/09544119211041417>.
- [6] T Mizutani, U Satake, T Enomoto. Bone grinding using coarse-grained diamond wheels to suppress thermal damage. *Precision Engineering-Journal of the International Societies for Precision Engineering and Nanotechnology*, 2022, 78: 163-170. <https://doi.org/10.1016/j.precisioneng.2022.08.003>.
- [7] M Yang, C H Li, L Luo, et al. Predictive model of convective heat transfer coefficient in bone micro-grinding using nanofluid aerosol cooling. *International Communications in Heat and Mass Transfer*, 2021, 125: 105317. <https://doi.org/10.1016/j.icheatmasstransfer.2021.105317>.
- [8] M Yang, M Kong, C H Li, et al. Temperature field model in surface grinding: A comparative assessment. *International Journal of Extreme Manufacturing*, 2023, <https://doi.org/10.1088/2631-7990/acf4d4>.
- [9] L Y Li, Y B Zhang, X Cui, et al. Mechanical behavior and modeling of grinding force: a comparative analysis. *Journal of Manufacturing Processes*, 2023, 102C: 921-954. <https://doi.org/10.1016/j.jmapro.2023.07.074>.
- [10] X T Zhang, C H Li, Z M Zhou, et al. Vegetable oil-based nanolubricants in machining: from physicochemical properties to application. *Chinese Journal of Mechanical Engineering*, 2023, 36: 76. <https://doi.org/10.1186/s10033-023-00895-5>.
- [11] W H Xu, C H Li, Y B Zhang, et al. Electrostatic atomization minimum quantity lubrication machining: from mechanism to application. *International Journal of Extreme Manufacturing*, 2022, 4(4): 042003. <https://doi.org/10.1088/2631-7990/ac9652>.
- [12] R P Singh, V Gupta, P M Pandey, et al. Effect of drilling techniques on microcracks and pull-out strength of cortical screw fixed in human tibia: An in-vitro study. *Annals of Biomedical Engineering*, 2021, 49(1): 382-393. <https://doi.org/10.1007/s10439-020-02565-2>.
- [13] Y Wang, M Cao, Y Y Zhao, et al. Experimental investigations on microcracks in vibrational and conventional drilling of cortical bone. *Journal of Nanomaterials*, 2013: 845205. <https://doi.org/10.1155/2013/845205>.
- [14] O B F J, T David, C L T. The effect of bone microstructure on the initiation and growth of microcracks. *Journal of Orthopaedic Research: Official Publication of the Orthopaedic Research Society*, 2005, 23(2): 475-480.
- [15] Z Zhu, Z W Hu, Z B Zang, et al. Study on grinding force of bovine cortical bone by different grinding wheels. *Diamond & Abrasives Engineering*, 2014, 34(5): 13-16, 28. (in Chinese) <https://doi.org/10.13394/j.cnki.jgssz.2014.5.0003>.
- [16] A Babbar, V Jain, D Gupta. In vivo evaluation of machining forces, torque, and bone quality during skull bone grinding. *Proceedings of the Institution of Mechanical Engineers Part H-Journal of Engineering in Medicine*, 2020, 234(6): 626-638. <https://doi.org/10.1177/0954411920911499>.
- [17] L H Zhang, L Zou, D H Wen, et al. Investigation of the effect of process parameters on bone grinding performance based on on-line measurement of temperature and force sensors. *Sensors*, 2020, 20(11): 3325. <https://doi.org/10.3390/s20113325>.
- [18] M Yang, C H Li, Z Said, et al. Semiempirical heat flux model of hard-brittle bone material in ductile microgrinding. *Journal of Manufacturing Processes*, 2021, 71: 501-514. <https://doi.org/10.1016/j.jmapro.2021.09.053>.
- [19] L Zhou, D H Wen, L H Zhang, et al. Computational model and experimental study for bone grinding force. *China Mechanical Engineering*, 2020, 31(24): 3016-3023. (in Chinese)
- [20] T Heqiang, Z Chenling, W Chenchen, et al. Modeling and simulation of a single abrasive grain micro-grinding force and temperature of bone. *Journal of Biomechanical Science and Engineering*, 2020, 15(4): 00012. <https://doi.org/10.1299/JBSE.20-00012>.
- [21] Y S Dambatta, C H Li, M Yang, et al. Grinding with minimum quantity lubrication: a comparative assessment. *International Journal of Advanced Manufacturing Technology*, 2023, 128(3-4): 955-1014. <https://doi.org/10.1007/s00170-023-11962-5>.
- [22] X M Wang, Y X Song, C H Li, et al. Nanofluids application in machining: a comprehensive review. *International Journal of Advanced Manufacturing Technology*, 2023, <https://doi.org/10.1007/s00170-022-10767-2>.
- [23] Z C Yang, L D Zhu, G X Zhang, et al. Review of ultrasonic vibration-assisted machining in advanced materials. *International Journal of Machine Tools & Manufacture*, 2020, 156: 103594. <https://doi.org/10.1016/j.ijmactools.2020.103594>.
- [24] L X Yao, Z Q Liu, Q H Song, et al. Prediction modelling of cutting force in rotary ultrasonic end grinding 2.5D woven SiO₂/SiO₂ ceramic matrix composite. *Composite Structures*, 2023, 304(1): 116448. <https://doi.org/10.1016/j.compstruct.2022.116448>.
- [25] T Gao, Y B Zhang, C H Li, et al. Fiber-reinforced composites in milling and grinding: machining bottlenecks and advanced strategies. *Frontiers of Mechanical Engineering*, 2022, 17(2): 24. <https://doi.org/10.1007/s11465-022-0680-8>.
- [26] H Wang, Z J Pei, W L Cong. A feeding-directional cutting force model for end surface grinding of CFRP composites using rotary ultrasonic machining with elliptical ultrasonic vibration. *International Journal of Machine Tools & Manufacture*, 2020, 152: 103540. <https://doi.org/10.1016/j.ijmactools.2020.103540>.
- [27] J H Zhang, Y Zhao, F Q Tian, et al. Kinematics and experimental study on ultrasonic vibration-assisted micro end grinding of silica glass. *International Journal of Advanced Manufacturing Technology*, 2015, 78(9-12): 1893-1904. <https://doi.org/10.1007/s00170-014-6761-z>.
- [28] H Wang, Z J Pei, W L Cong. A mechanistic cutting force model based on ductile and brittle fracture material removal modes for edge surface grinding of CFRP composites using rotary ultrasonic machining. *International Journal of Mechanical Sciences*, 2020, 176: 105551. <https://doi.org/10.1016/j.ijmecsci.2020.105551>.
- [29] X Z Xiao, K Zheng, W H Liao, et al. Study on cutting force model in ultrasonic vibration assisted side grinding of zirconia ceramics. *International Journal of Machine Tools & Manufacture*, 2016, 104: 58-67. <https://doi.org/10.1016/j.ijmactools.2016.01.004>.
- [30] Z C Yang, L D Zhu, C B Ni, et al. Investigation of surface topography formation mechanism based on abrasive-workpiece contact rate model in tangential ultrasonic vibration-assisted CBN grinding of ZrO₂ ceramics. *International Journal of Mechanical Sciences*, 2019, 155: 66-82. <https://doi.org/10.1016/j.ijmecsci.2019.02.031>.
- [31] Z Li, S M Yuan, H Song, et al. A cutting force model based on kinematics analysis for C/SiC in rotary ultrasonic face machining. *International Journal of Advanced Manufacturing Technology*, 2018, 97(1-4): 1223-1239. <https://doi.org/10.1007/s00170-018-1995-9>.
- [32] M Yang, C H Li, Y B Zhang, et al. Experimental research on microscale grinding temperature under different nanoparticle jet minimum quantity cooling. *Materials and Manufacturing Processes*, 2017, 32(6): 589-597. <https://doi.org/10.1080/10426914.2016.1176198>.
- [33] Y Y Yang, M Yang, C H Li, et al. Machinability of ultrasonic vibration-assisted micro-grinding in biological bone using nanolubricant. *Frontiers of Mechanical Engineering*, 2023, 18(1): <https://doi.org/10.1007/s11465-022-0717-z>.
- [34] T Gao, C H Li, Y B Zhang, et al. Mechanical behavior of material removal and predictive force model for CFRP grinding using nano reinforced biological lubricant. *Journal of Mechanical Engineering*, 2023, 59(13): 325-342. (in Chinese)

- [35] M Z Liu, C H Li, Y B Zhang, et al. Analysis of grinding mechanics and improved grinding force model based on randomized grain geometric characteristics. *Chinese Journal of Aeronautics*, 2023, 36(7): 160-193. <https://doi.org/10.1016/j.cja.2022.11.005>.
- [36] M Z Liu, C H Li, Y B Zhang, et al. Analysis of grain tribology and improved grinding temperature model based on discrete heat source. *Tribology International*, 2023, 180:108196 <https://doi.org/10.1016/j.triboint.2022.108196>.
- [37] B T Huang, C H Li, Y B Zhang, et al. Advances in fabrication of ceramic corundum abrasives based on sol-gel process. *Chinese Journal of Aeronautics*, 2021, 34(6): 1-17. <https://doi.org/10.1016/j.cja.2020.07.004>.
- [38] C J Wu, B Z Li, Y Liu, et al. Surface roughness modeling for grinding of Silicon Carbide ceramics considering co-existence of brittleness and ductility. *International Journal of Mechanical Sciences*, 2017, 133: 167-177. <https://doi.org/10.1016/j.ijmecsci.2017.07.061>.
- [39] S S Qu, Y D Gong, Y Y Yang, et al. Mechanical model and removal mechanism of unidirectional carbon fibre-reinforced ceramic composites. *International Journal of Mechanical Sciences*, 2020, 173: 105465. <https://doi.org/10.1016/j.ijmecsci.2020.105465>.
- [40] C M Zhu, P Gu, Y Y Wu, et al. Surface roughness prediction model of SiCp/Al composite in grinding. *International Journal of Mechanical Sciences*, 2019, 155: 98-109. <https://doi.org/10.1016/j.ijmecsci.2019.02.025>.
- [41] R L Hecker, S Y Liang, X J Wu, et al. Grinding force and power modeling based on chip thickness analysis. *The International Journal of Advanced Manufacturing Technology*, 2007, 33(5-6): <https://doi.org/10.1007/s00170-006-0473-y>.
- [42] X H Zhang, Z X Kang, S Li, et al. Grinding force modelling for ductile-brittle transition in laser macro-micro-structured grinding of zirconia ceramics. *Ceramics International*, 2019, 45(15): 18487-18500. <https://doi.org/10.1016/j.ceramint.2019.06.067>.
- [43] R K Kang, J T Liu, Z G Dong, et al. An Improved Cutting Force Model for Ultrasonically Assisted Grinding of Hard and Brittle Materials. *Applied Sciences-Basel*, 2021, 11(9): 3888. <https://doi.org/10.3390/app11093888>.
- [44] M Yang, CH Li, YB Zhang, et al. Theoretical analysis and experimental research on temperature field of microscale bone grinding under nanoparticle jet mist cooling. *Journal of Mechanical Engineering*, 2018, 54(18): 194-203. (in Chinese)
- [45] Y G Zhou, C C Tian, S Q Jia, et al. Study on grinding force of two-dimensional ultrasonic vibration grinding 2.5D-C/SiC composite material. *Crystals*, 2023, 13(1):151. <https://doi.org/10.3390/cryst13010151>.
- [46] P Liu, S C Mao, L H Wang, et al. Direct dynamic atomic mechanisms of strain-induced grain rotation in nanocrystalline, textured, columnar-structured thin gold films. *Scripta Materialia*, 2011, 64(4): 343-346. <https://doi.org/10.1016/j.scriptamat.2010.10.029>.
- [47] C Li, X L Li, Y Q Wu, et al. Deformation mechanism and force modelling of the grinding of YAG single crystals. *International Journal of Machine Tools & Manufacture*, 2019, 143:23-37. <https://doi.org/10.1016/j.ijmactools.2019.05.003>.
- [48] Z D Zheng, K Huang, C T Lin, et al. An analytical force and energy model for ductile-brittle transition in ultra-precision grinding of brittle materials. *International Journal of Mechanical Sciences*, 2022, 220: 107107. <https://doi.org/10.1016/j.ijmecsci.2022.107107>.
- [49] Y Zhang, J A Robles-Linares, L Chen, et al. Advances in machining of hard tissues-From material removal mechanisms to tooling solutions. *International Journal of Machine Tools & Manufacture*, 2022, 172: 103838. <https://doi.org/10.1016/j.ijmactools.2021.103838>.
- [50] Y Wang, B Lin, S L Wang, et al. Study on the system matching of ultrasonic vibration assisted grinding for hard and brittle materials processing. *International Journal of Machine Tools & Manufacture*, 2014, 77:66-73. <https://doi.org/10.1016/j.ijmactools.2013.11.003>.
- [51] Z K Zhang, S M Yuan, X X Gao, et al. Analytical modelling of side grinding of orthogonal laminated SiCf/SiC composites based on effective elastic properties. *International Journal of Advanced Manufacturing Technology*, 2022, 120(9-10): 6419-6434. <https://doi.org/10.1007/s00170-022-09170-8>.
- [52] B Lawn, R Wilshaw. Indentation fracture: principles and applications. *Journal of Materials Science*, 1975, 10(6): <https://doi.org/10.1007/BF00823224>.
- [53] G C Qiao, Z Cheng, W Zheng, et al. Grinding force model for longitudinal-torsional ultrasonic-assisted face grinding of ceramic matrix composites. *International Journal of Advanced Manufacturing Technology*, 2022, 120(11-12): 7721-7733. <https://doi.org/10.1007/s00170-022-09174-4>.
- [54] Z P Li, F H Zhang, X C Luo, et al. A new grinding force model for micro grinding RB-SiC ceramic with grinding wheel topography as an input. *Micromachines*, 2018, 9(8): 368. <https://doi.org/10.3390/mi9080368>.
- [55] F H Zhang, B B Meng, Y Q Geng, et al. Friction behavior in nanoscratching of reaction bonded silicon carbide ceramic with Berkovich and sphere indenters. *Tribology International*, 2016, 97: 21-30. <https://doi.org/10.1016/j.triboint.2016.01.013>.
- [56] M Yang, C H Li, Y B Zhang, et al. Maximum undeformed equivalent chip thickness for ductile-brittle transition of zirconia ceramics under different lubrication conditions. *International Journal of Machine Tools & Manufacture*, 2017, 122: 55-65. <https://doi.org/10.1016/j.ijmactools.2017.06.003>.
- [57] M Yang, C H Li, Y B Zhang, et al. A new model for predicting neurosurgery skull bone grinding temperature field. *Journal of Mechanical Engineering*, 2018, 54(23): 215-222. (in Chinese)
- [58] Z R Liao, D A Axinte. On chip formation mechanism in orthogonal cutting of bone. *International Journal of Machine Tools & Manufacture*, 2016, 102: 41-55. <https://doi.org/10.1016/j.ijmactools.2015.12.004>.
- [59] C Santiuste, M Rodriguez-Millan, E Giner, et al. The influence of anisotropy in numerical modeling of orthogonal cutting of cortical bone. *Composite Structures*, 2014, 116: 423-431. <https://doi.org/10.1016/j.compstruct.2014.05.031>.
- [60] ZR Liao. *Research on bone cutting and a novel tool development*. Harbin: Harbin Institute of Technology, 2017. (in Chinese)
- [61] V Tahmasbi, M Qasemi, R Ghasemi, et al. Experimental study and sensitivity analysis of force behavior in cortical bone milling. *Medical Engineering & Physics*, 2022, 105: 103821. <https://doi.org/10.1016/j.medengphy.2022.103821>.
- [62] S Li. Study of human bone hardness atlas and the relationship between bone hardness and biomechanical properties [doctor]. *Hebei Medical University*, 2021. (in Chinese)
- [63] Z Zhu. *Experimental study on bone tissue grinding characteristics*. Quanzhou: Huaqiao University, 2014. (in Chinese)
- [64] W Q Lin, Li GX. Fracture mechanics and fracture of bone. *International Journal of Biomedical Engineering*, 1982(4): 211-216. (in Chinese)
- [65] Z R Liao, D Axinte, D Gao. On modelling of cutting force and temperature in bone milling. *Journal of Materials Processing Technology*, 2019, 266: 627-638. <https://doi.org/10.1016/j.jmatprotec.2018.11.039>.
- [66] L Salguero, F Saadat, I Sevostianov. Micromechanical modeling of elastic properties of cortical bone accounting for anisotropy of dense tissue. *Journal of Biomechanics*, 2014, 47(13): 3279-3287. <https://doi.org/10.1016/j.jbiomech.2014.08.019>.
- [67] N Reznikov, R Shahar, S Weiner. Bone hierarchical structure in three dimensions. *Acta Biomaterialia*, 2014, 10(9): 3815-3826. <https://doi.org/10.1016/j.actbio.2014.05.024>.
- [68] F Hamandi, J T Tsatalis, T Goswami. Retrospective evaluation and framework development of bone anisotropic material behavior compared with elastic, elastic-plastic, and hyper-elastic properties. *Bioengineering-Basel*, 2022, 9(1): 9. <https://doi.org/10.3390/bioengineering9010009>.

Submit your manuscript to a SpringerOpen[®] journal and benefit from:

- Convenient online submission
- Rigorous peer review
- Open access: articles freely available online
- High visibility within the field
- Retaining the copyright to your article

Submit your next manuscript at ► [springeropen.com](https://www.springeropen.com)